RESTORECT: DEGRADED IMAGE RESTORATION VIA LATENT RECTIFIED FLOW & FEATURE DISTILLATION

Anonymous authors
Paper under double-blind review

ABSTRACT

Current approaches for restoration of degraded images face a critical trade-off: high-performance models are too slow for practical use, while fast models produce poor results. Knowledge distillation transfers teacher knowledge to students, but existing static feature matching methods cannot capture how modern transformer architectures dynamically generate features. We propose **'RestoRect'**, a novel Latent Rectified Flow Feature Distillation method for restoring degraded images. We apply rectified flow to reformulate feature distillation as a generative process where students learn to synthesize teacher-quality features through learnable trajectories in latent space. Our framework combines Retinex theory for physics-based decomposition with learnable anisotropic diffusion constraints, and trigonometric color space polarization. We introduce a Feature Layer Extraction loss for robust knowledge transfer between different network architectures through cross-normalized transformer feature alignment with percentile-based outlier detection. RestoRect achieves better training stability, and faster convergence and inference while preserving restoration quality. We demonstrate superior results across 15 image restoration datasets, covering 4 tasks, on 10 metrics.

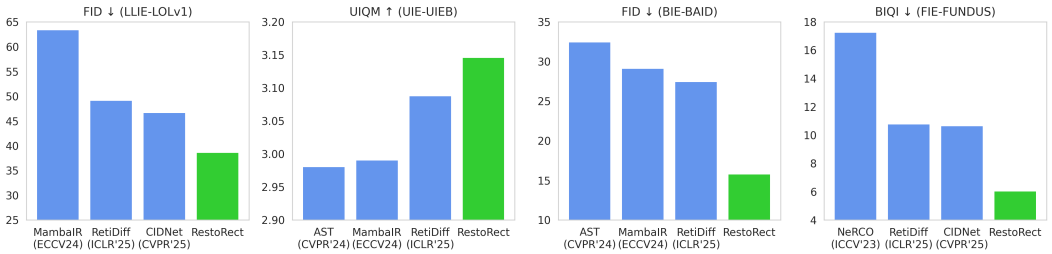

Figure 1: RestoRect achieves superior performance on four image restoration tasks.

1 INTRODUCTION

Image restoration from degraded inputs including low-light (LLIE), underwater (UIE), backlit (BAID), and fundus (FIE) enhancement, remains a key challenge in computer vision. Real-world images often suffer from illumination degradation, noise, and compression artifacts that impair both human perception and downstream tasks. Traditional optimization-based methods exploit physical priors but falter on images with complex degradations, while transformer-based deep learning achieves strong restoration by learning rich multi-scale features. Generative approaches further enhance quality, with diffusion models operating in latent spaces and integrating Retinex priors to capture the complex distributions of natural images. However, such gains incur steep computational costs, limiting real-time use. Knowledge distillation offers efficiency by transferring knowledge from large teachers to compact students, but struggles with transformer-based restoration. Conventional approaches compute static feature losses between teacher and student layers, neglecting the dynamic feature generation of multi-head attention and layer interactions. This mismatch hampers dependency modeling, degrading student performance. Recent models such as Reti-Diff (He et al., 2023) (Retinex priors) and HVI-CIDNet (Yan et al., 2024) (learnable color spaces) achieve good restoration, but their distillation relies on static feature matching, which fails to capture generative processes.

We propose **RestoRect**, which formulates knowledge distillation as a generative process through latent rectified flow. Instead of matching static features, student networks learn the dynamic synthesis of features through flow matching dynamics, using linear interpolation trajectories in latent space between noise and target features. This reduces sampling steps while preserving feature quality.

At the core of RestoRect is the **F**eature **L**ayer **EX**traction (FLEX) Loss, designed to address distribution mismatch in feature distillation. Unlike prior methods that assume teacher and student features share the same statistical space, FLEX normalizes both using student statistics, enabling meaningful comparison despite evolving feature distributions during training. To further stabilize learning, percentile-based outlier detection mitigates noisy or corrupted regions. Our framework integrates classical image processing with modern generative modeling: Retinex theory for physics-based decomposition, learnable anisotropic diffusion for structural consistency, and trigonometric color space polarization to eliminate the red discontinuity artifacts common in image transformations. Together, these components preserve both texture and color in restored images.

RestoRect employs a two-stage training paradigm for feature distillation. In Stage 1, the teacher network is trained with pixel, perceptual, and physics-based losses to achieve high-quality restoration. Stage 2 distills knowledge into the student via latent rectified flow. In its first phase, only rectified flow velocity predictors are trained while the main restoration network remains frozen. The pre-trained teacher extracts high-quality Retinex and image features from paired degraded and ground-truth inputs, which serve as targets for two rectified flow models. These models learn velocity fields that reproduce teacher-level features through learnable trajectories, enabling synthesis in only a few steps. In the second phase, the full restoration network is trained using these generative processes: velocity predictors dynamically generate student features, which are aligned with teacher features via our FLEX Loss that cross-normalizes multi-scale transformer representations and applies percentile-based outlier detection. This design allows the student to efficiently learn and generate teacher-quality features, achieving restoration performance comparable to diffusion-based methods while operating at significantly higher efficiency.

Our key technical contributions include: **1.** A novel framework modeling knowledge transfer as a generative process using latent rectified flow, where the student network learns velocity fields to synthesize teacher-quality features. **2.** A novel U-Net transformer architecture with Spatial Channel Layer Normalization (SCLN) and Query-Key normalization, for attention stability under degraded inputs. **3.** A novel Feature Layer EXtraction (FLEX) Loss using feature statistics to normalize both teacher and student representations for multi-scale alignment in transformers. **4.** Combining Retinex theory with learnable anisotropic diffusion constraints and trigonometric color space polarization to eliminate artifacts and boost restoration quality.

2 Related Work

Degraded Image Restoration has evolved from classical signal processing to modern deep learning frameworks. Early approaches such as histogram equalization (Cheng & Shi, 2004), gamma correction (Huang et al., 2012), and Retinex theory (Edwin, 1977) provided interpretable solutions but failed to generalize across degradations. Retinex-based extensions (Fu et al., 2016; Li et al., 2018) incorporated physical priors for reflectance–illumination decomposition, yet remained constrained by hand-crafted assumptions. Deep learning enabled data-driven feature learning, with convolutional models by (Wei et al., 2018) and by (Wang et al., 2019) leveraging Retinex decomposition for improved color correction. Transformer-based methods further enhanced global illumination consistency (Zamir et al., 2022), while adaptive designs by (Xu et al., 2022) and state space models like by (Guo et al., 2024) advanced efficiency and context modeling. Specialized solutions addressed low-light enhancement (Guo et al., 2020; Jiang et al., 2021), underwater restoration (Naik et al., 2021; Guo et al., 2023), and backlit enhancement (Gaintseva et al., 2024; Jiang et al., 2021). Hybrid approaches such as by (He et al., 2025b) bridged optimization- and learning-based paradigms via deep unfolding, while by (Yan et al., 2024; 2025) introduced learnable color-space transformations to decouple brightness and chromaticity.

Image Generative Modeling aims to capture complex data distributions and synthesize realistic details. GAN-based methods (Cong et al., 2023; Jiang et al., 2021) achieved high-quality results but suffered from instability and mode collapse. Diffusion models improved fidelity through iterative denoising (Yi et al., 2023), though efficiency remained limited. Latent-space diffusion, such as Reti-

Diff (He et al., 2023), reduced overhead by incorporating Retinex priors. Flow-based approaches offered exact likelihoods and stable training (Kingma & Dhariwal, 2018), with rectified flow (Liu et al., 2022) enabling efficient straight-line sampling. Integrating generative priors into restoration networks has driven advances in knowledge distillation (Hinton et al., 2015), conditional and multi-scale generation (Saharia et al., 2022; Ho et al., 2022), and physics-informed restoration (Xia et al., 2023). Nonetheless, achieving real-time, high-fidelity restoration remains challenging due to the trade-off between generative quality and computational efficiency.

Knowledge Distillation enables compact models to inherit capabilities from larger teachers (Hinton et al., 2015). Early methods matched intermediate features (Romero et al., 2014) or attention maps (Zagoruyko & Komodakis, 2016), using L2 losses (Heo et al., 2019) or attention transfer (Huang & Wang, 2017). For vision transformers, challenges from multi-head attention and positional encodings inspired approaches like distillation tokens in DeiT (Touvron et al., 2021) and attention matrix alignment (Wang et al., 2020). However, these strategies treat features as static targets, overlooking the dynamic generation in transformer architectures (Jiao et al., 2019). In image restoration, distillation is further complicated by multi-scale feature dependencies and complex distributions (Zhang et al., 2022; Berrada et al., 2025). Architectural mismatches between teacher and student amplify these gaps, limiting transfer efficiency and degrading restoration quality, motivating new paradigms that model feature generation as a learnable process rather than static matching (Bing et al., 2025).

3 Methodology

3.1 Problem Formulation

We tackle efficient knowledge distillation for degraded image restoration, aiming to transfer knowledge from a powerful teacher $\mathcal{F}_T$ to a lightweight student $\mathcal{F}_S$ without sacrificing quality. Given a degraded input $I_{LQ} \in \mathbb{R}^{H\times W\times 3}$ and ground truth $I_{GT} \in \mathbb{R}^{H\times W\times 3}$, the objective is: $\mathcal{F}_S(I_{LQ}) \approx \mathcal{F}_T(I_{LQ}) \approx I_{GT}$. The main challenge is feature distribution mismatch between teacher and student. Standard distillation aligns features with simple distance metrics, which breaks down when distributions differ significantly, especially in transformer-based networks where multi-head attention produces features with varying means, variances, and outlier characteristics.

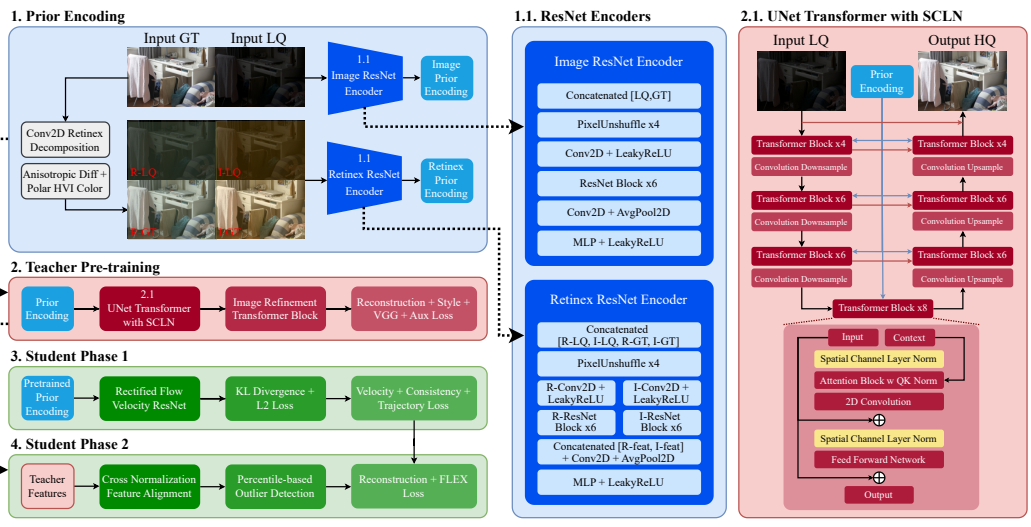

Figure 2: Training framework flowchart for RestoRect. Starting from top left (1. Prior Encoding) the inputs go through retinex decomposition and pass through encoders (1.1 ResNet Encoders) to prepare image and retinex prior encodings. Next these prior encodings are pre-trained (2. Teacher Pre-training) with the teacher model (2.2 UNet Transformer with SCLN) using a reconstruction loss. Finally the frozen prior encodings and teacher model are used for student phase 1 and phase 2 training using rectified flow loss. Full architecture details in Appendix A.7.

3.2 TEACHER NETWORK TRANSFORMER PRETRAINING

Our method uses well-established Retinex theory to derive physics-informed features as priors for knowledge distillation. Retinex models an image I as the product of reflectance R and illumination L: $I = R \odot L$, where R encodes surface properties and L captures lighting. We use two decomposition networks, $\mathcal{D}_l$ (low-light) and $\mathcal{D}_h$ (normal-light), each mapping $\mathcal{D}(I) \to (R, L)$ with $R \in \mathbb{R}^{H\times W\times 3}$ and $L \in \mathbb{R}^{H\times W\times 1}$ (Wu et al., 2022; He et al., 2023). This dual setup ensures robust decomposition under diverse lighting. The decomposed components are then encoded (Figure 2(1)): a Retinex encoder extracts features from $[R; L]$ via reflectance (192-dim) and illumination (64-dim) pathways, while an image encoder processes raw image features to preserve holistic appearance. Our teacher network uses U-Net transformer architecture (Huang et al., 2020; Cao et al., 2022) with key innovations for robust image restoration. The hierarchical transformer architecture processes multi-scale representations through encoder-decoder structures with skip connections, incorporating specialized normalization and attention mechanisms designed for degraded image inputs. Traditional layer normalization operates independently on spatial and channel dimensions, potentially losing critical spatial correlations essential for restoration tasks.

Spatial Channel Layer Normalization (SCLN) is introduced that captures global image statistics: $\text{SCLN}(x) = (x - \mu_{global})/(\sqrt{\sigma^2_{global} + \epsilon}) \cdot \gamma$, where the global statistics are computed across flattened spatial-channel dimensions. This novel formulation ensures that normalization captures both local spatial patterns and global image characteristics, with learnable channel-wise scaling $\gamma \in \mathbb{R}^C$ that adapts to different feature semantics. Transformer-based restoration suffers from attention instability during training, particularly with degraded inputs which have irregular noise patterns and missing information. We apply normalization to query and key representations before attention computation, which prevents attention weight saturation in degraded regions, and ensures stable gradients throughout the attention mechanism: $\text{Attn}(Q, K, V) = \text{softmax}\left(\frac{\text{Norm}(Q)\cdot\text{Norm}(K)^T}{\sqrt{d_k}} \cdot \tau\right) V$. The teacher network processes both raw images and their Retinex decompositions through separate pathways. This design allows queries from reflectance components to attend to illumination structure, preserving intrinsic scene properties. Figure 3 shows in blue our SCLN with QK norm achieves more stable training compared to vanilla layer normalization without QK norm in red. To our knowledge no previous restoration method has used this transformer architecture.

Table 1: Computational overhead comparison between LayerNorm (LN) and Spatial Channel Layer Norm (SCLN) across different precisions on an MLP network. Results averaged over 3 random seeds on 512×512×64 resolution.

	Single Layer Performance (ms)				Multi-layer Performance (ms)			
Precision	**LayerNorm**	**SCLN**	**Overhead**	**(%)**	**LayerNorm**	**SCLN**	**Overhead**	**(%)**
FP32	0.7059 ± 0.0004	0.7113 ± 0.0000	0.0054	+0.76	3.05 ± 0.00	3.06 ± 0.00	0.01	+0.33
FP16	0.1899 ± 0.0000	0.1991 ± 0.0001	0.0092	+4.82	1.21 ± 0.00	1.17 ± 0.00	−0.05	−3.72
BF16	0.1935 ± 0.0001	0.2004 ± 0.0001	0.0069	+3.57	1.23 ± 0.00	1.17 ± 0.00	−0.06	−4.67

The benchmark results in Table 1 show that SCLN introduces minimal computational overhead due to its efficient normalization strategy. At the single-layer level, SCLN incurs only 0.76% overhead in FP32, as computing statistics across spatial-channel dimensions requires marginally more operations than channel-wise normalization. The slightly higher percentage overhead in FP16/BF16 (4.82% and 3.57%) is primarily an artifact of the dramatically reduced absolute inference times, LayerNorm executes so quickly in lower precision that even negligible absolute differences appear larger percentagewise. At the full network level, SCLN's overhead becomes negligible (0.33% in FP32) or even negative (-3.72% in FP16, -4.67% in BF16), suggesting superior memory access patterns and cache efficiency when operations are repeated across multiple layers. Standard LayerNorm's repeated reshape operations (to_3d/to_4d conversions) accumulate overhead, while SCLN's direct 4D tensor operations benefit from better spatial locality and reduced memory bandwidth pressure. This explains why SCLN actually becomes faster than LayerNorm in lower-precision full-network scenarios, making the trade-off highly favorable with PSNR improvement with no speed penalty. Note that we train our RestoRect models with FP32, and Table 1 is a toy MLP example.

Auxiliary Constraints like anisotropic diffusion (Perona et al., 1994) and polarized HVI color spaces (Yan et al., 2024) (Yan et al., 2025) are incorporated that enforce edge-preserving texture matching and eliminate artifacts. The anisotropic diffusion operator computes: $\mathcal{A}(I) = \nabla \cdot (c(|\nabla I|)\nabla I)$, with the diffusion coefficient defined as: $c(|\nabla I|) = \exp\left(-|\nabla I|^2/s^2\right)$, where s is a learnable sensitivity parameter initialized as $s = 0.1$ and constrained to $s \in [0.01, 1.0]$ to prevent numerical instability. The texture consistency loss enforces structural similarity between input and predicted reflectance: $L_{tex} = \|\mathcal{A}(I_{input}) - \mathcal{A}(R_{pred})\|_1$. This constraint preserves essential edge structures while suppressing noise, maintains texture coherence across different scales, and provides gradient-based supervision for fine-grained details. We additionally enforce illumination smoothness through gradient-aware weighting: $L_{lum} = \sum_{i,j} w_{i,j} \left(|\nabla_x L_{i,j}|^2 + |\nabla_y L_{i,j}|^2\right)$, where $w_{i,j} = \exp(-|\nabla L_{i,j}|)$ provides adaptive regularization based on local gradient magnitude. Standard image color spaces exhibit critical limitations for restoration like discontinuities at the red boundary ($H = 0°$ and $H = 360°$) and degenerate mappings in dark regions. To address these fundamental limitations, polarized HVI (Horizontal-Vertical-Intensity) color space is introduced that eliminates these artifacts through trigonometric parameterization. The polarized transformation maps hue to continuous coordinates: $H_{polar} = C_k \cdot S \cdot \cos(\pi H/3), V_{polar} = C_k \cdot S \cdot \sin(\pi H/3), I_{polar} = I_{max} = \max(R, G, B)$, where the adaptive intensity collapse factor is: $C_k = k \cdot \sin(\pi I_{max}/2) + \epsilon$, with learnable density parameter k initialized to 1.0 and constrained to $k \in [0.1, 5.0]$. This formulation eliminates red discontinuity through periodic parameterization, provides robustness through adaptive intensity collapse that prevents degenerate mappings in dark regions, and maintains color relationships under illumination changes. While (Yan et al., 2024) (Yan et al., 2025) frames HVI as a representation transformation, we define an explicit color loss in HVI space. The polarized color loss is computed as:

$$L_{col} = \|H^{pred}_{polar} - H^{gt}_{polar}\|_1 + \|V^{pred}_{polar} - V^{gt}_{polar}\|_1 + \|I^{pred}_{polar} - I^{gt}_{polar}\|_1 \tag{1}$$

The primary reconstruction objective employs pixel-wise supervision through L1 loss: $L_{rec} = \|I_{pred} - I_{gt}\|_1$, where I_{pred} represents the network's restored output and I_{gt} denotes the ground truth high-quality image. To capture perceptual similarity beyond pixel-level differences, we incorporate perceptual loss using pre-trained VGG (Simonyan & Zisserman, 2014)features. The perceptual loss extracts multi-scale feature representations that align with human visual perception: $L_{vgg} = \sum_l \lambda_l \|\phi_l(I_{pred}) - \phi_l(I_{gt})\|_2^2$, where ϕ_l represents VGG features at layer l, and λ_l denotes layer-specific weights that emphasize semantically important features. We additionally incorporate style loss that captures texture and artistic consistency through Gram matrix matching: $L_{sty} = \sum_l \|G_l(\phi_l(I_{pred})) - G_l(\phi_l(I_{gt}))\|_F^2$, where $G_l(\phi_l(I)) = \phi_l(I)\phi_l(I)^T$ computes the Gram matrix at layer l, and $\|\cdot\|_F$ denotes the Frobenius norm. This novel combination ensures that the restored images maintain both structural accuracy and perceptual realism. The complete teacher training objective combines these losses:

$$L_{teach} = L_{rec} + L_{vgg} + L_{sty} + \lambda_{tex} L_{tex} + \lambda_{col} L_{col} + \lambda_{lum} L_{lum} \tag{2}$$

with $\lambda_{tex} = 0.05$, $\lambda_{col} = 0.05$, and $\lambda_{lum} = 0.2$. Figure 3 shows in green our how our auxiliary constraints allow training of a stronger teacher model with faster convergence. (He et al., 2023) previously used reconstruction and style loss with perceptual VGG features. To our knowledge, we are the first to implement anisotropic diffusion texture and illumination smoothness constraints with explicit HVI color loss.

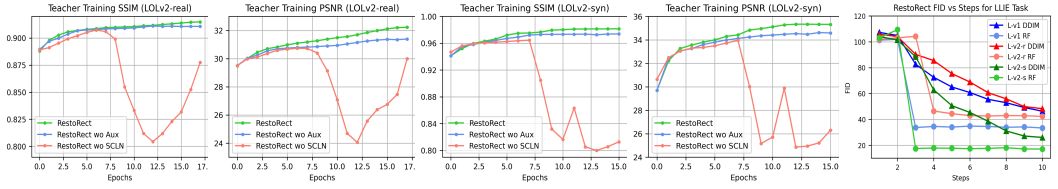

Figure 3: (1-4) Teacher model training with ablations of SCLN & QK Norm (red) and auxiliary losses (blue). (5) FID vs Steps inference performance show Rectified Flow (RF) student model producing high quality images in fewer steps compared to Denoising Diffusion Implicit Model (DDIM).

3.3 STUDENT NETWORK TRAINING WITH LATENT RECTIFIED FLOW

Traditional knowledge distillation treats feature transfer as static matching between teacher and student representations. This approach suffers from several limitations including assuming compatible feature distributions between architectures, lacking flexibility in handling multi-modal feature distributions, and being unable to adapt to varying complexity of restoration tasks. We reformulate knowledge distillation as a generative process using rectified flow, which models feature synthesis through straight-line paths in latent space. Given teacher features $\mathbf{f}_{teach} \in \mathbb{R}^d$ and noise $\mathbf{z} \sim \mathcal{N}(0, I)$, rectified flow defines the interpolation path: $\mathbf{x}_t = (1-t)\mathbf{z} + t\mathbf{f}_{teach}, \quad t \in [0,1]$. The velocity field represents the direction of optimal transport: $\mathbf{v}(\mathbf{x}_t, t) = \frac{d\mathbf{x}_t}{dt} = \mathbf{f}_{teach} - \mathbf{z}$. We train separate velocity prediction networks ϵ_θ^{ref} and ϵ_θ^{img} for reflectance and image features using the velocity matching objective: $L_{vel} = \mathbb{E}_{t,\mathbf{z},\mathbf{f}_{teach}}\left[\|\epsilon_\theta(\mathbf{x}_t, t, \mathbf{c}) - \mathbf{v}(\mathbf{x}_t, t)\|_2^2\right]$, where $\mathbf{c}$ represents conditioning information from the input image. Each velocity predictor implements a Residual MLP architecture. During inference, we solve the ODE using Euler's method with adaptive step sizing: $\mathbf{x}_{t+\Delta t} = \mathbf{x}_t + \Delta t \cdot \epsilon_\theta(\mathbf{x}_t, t, \mathbf{c})$. This requires only 1-4 integration steps compared to 10+ steps for DDIM models, providing significant computational advantages. Standard knowledge distillation losses (KL divergence, L2 distance) assume that teacher and student features exist in compatible statistical distributions. This assumption fails for complex transformer architectures, and when finetuning on different datasets, leading to suboptimal knowledge transfer (Lin et al., 2022).

FLEX (Feature Layer EXtraction) Loss addresses feature distribution mismatch through cross-normalization for distribution alignment, percentile-based outlier detection for robust training, and dynamic resolution-aware weighting for multi-scale importance. Unlike (Berrada et al., 2025) which is specialized for diffusion autoencoders, FLEX provides a general-purpose distillation loss that transfers feature distributions across heterogeneous teacher-student architectures. The key method is cross-normalization using student statistics. For each layer l, FLEX normalizes both teacher and student features using student statistics:

$$\mu_{\text{stud}}^l = \text{mean}(\mathbf{f}_{\text{stud}}^l), \quad \sigma_{\text{stud}}^l = \text{std}(\mathbf{f}_{\text{stud}}^l) + \epsilon, \quad \mathbf{f}_{\text{teach}}^{l,\text{norm}} = \frac{\mathbf{f}_{\text{teach}}^l - \mu_{\text{stud}}^l}{\sigma_{\text{stud}}^l}, \quad \mathbf{f}_{\text{stud}}^{l,\text{norm}} = \frac{\mathbf{f}_{\text{stud}}^l - \mu_{\text{stud}}^l}{\sigma_{\text{stud}}^l}$$

This aligns both features to the student's distribution, enabling meaningful comparison across architecture capacity differences. FLEX incorporates fast percentile-based outlier detection to handle extreme values that destabilize training. This masking strategy prioritizes training stability over complete spatial coverage, as extreme outliers generate destabilizing gradients that outweigh their informational value. The outlier mask identifies reliable spatial locations: $M_{\text{reliable}}^{l,c,h,w} = \mathbb{I}[|\mathbf{f}_{\text{stud}}^{l,c,\text{norm},h,w}| \leq \tau_p^{l,c}]$, where $\tau_p^{l,c}$ is the p-th percentile of normalized feature magnitudes for layer l, channel c, with p=95% by default. FLEX computes dynamic resolution-based weights:

$$w_l^{\text{res}} = \max\left((H_{\text{base}} W_{\text{base}} / H_l W_l)^{0.25}, 0.1\right)$$

where $(H_{\text{base}}, W_{\text{base}}) = (64, 64)$ ensures appropriate weighting across resolutions. The complete FLEX loss combines masked feature matching with dual weighting:

$$L_{\text{FLEX}} = \sum_l w_l^{\text{layer}} \cdot w_l^{\text{res}} \cdot \frac{\sum_{c,h,w} M_{\text{reliable}}^{l,c,h,w} \cdot \|\mathbf{f}_{\text{teach}}^{l,c,\text{norm},h,w} - \mathbf{f}_{\text{stud}}^{l,c,\text{norm},h,w}\|^2}{\sum_{c,h,w} M_{\text{reliable}}^{l,c,h,w} + \epsilon} \tag{3}$$

where w_l^{layer} represents predefined layer weights and the denominator normalizes by reliable elements. FLEX includes SNR-aware application, activating only when $t/T < \tau_{\text{SNR}} = 0.4$, focusing distillation on cleaner intermediate states. Cross-normalization enables stable transfer between different architectures, outlier detection prevents training instability, dynamic weighting balances multi-scale contributions, and streaming processing optimizes memory usage. Standard KD methods lack these capabilities, assuming compatible distributions and uniform spatial weighting.

Trajectory Consistency Regularization is introduced to ensure smooth and semantically consistent rectified flow trajectories, which prevents erratic feature generation and maintains coherence throughout the ODE integration process (Yang et al., 2024). We enforce smooth transitions between consecutive ODE steps: $L_{trans} = \sum_{i=1}^{N-1} \|\mathbf{f}_{pred}^{i+1} - \mathbf{f}_{pred}^i\|_2^2$, where $\mathbf{f}_{pred}^i$ represents predicted features at the i-th integration step. We ensure final generated features align with teacher targets: $L_{target} = \|\mathbf{f}_{pred}^{final} - \mathbf{f}_{teach}\|_2^2$. We enforce consistency in semantic feature representations across

the trajectory: $L_{cons} = \sum_{i=1}^{N} \text{cos\_dist}(\mathbf{f}_{pred}^{i}, \mathbf{f}_{teach})$. The complete trajectory consistency loss is: $L_{traj} = \alpha_{trans} L_{trans} + \alpha_{target} L_{target} + \alpha_{cons} L_{cons}$, with $\alpha_{trans} = 0.1$, $\alpha_{target} = 0.5$, and $\alpha_{cons} = 0.2$. Our training protocol addresses the challenge of jointly learning velocity prediction and restoration quality through a principled two-phase approach. We first train rectified flow components while freezing the main restoration network:

$$L_{phase1} = L_{vel}^{rex} + L_{vel}^{img} + \lambda_{KD} L_{KD} + \lambda_{traj} L_{traj} \tag{4}$$

This phase establishes stable velocity prediction capabilities without interference from restoration objective gradients. We use separate optimizers for reflectance and image velocity predictors with learning rates $lr_{rex} = 2 \times 10^{-4}$ and $lr_{img} = 2 \times 10^{-4}$. The complete network is then trained using features generated by learned velocity predictors, where $\lambda_{FLEX} = 0.15$, $\lambda_{vel} = 0.05$:

$$L_{phase2} = L_{rec} + \lambda_{FLEX} L_{FLEX} + \lambda_{vel}(L_{vel}^{rex} + L_{vel}^{img}) \tag{5}$$

4 Experiments

Experimental Setup. We implement our model in PyTorch and trained it on 8 NVIDIA H100 GPUs. Teacher pretraining is performed for 15-20 epochs depending on dataset convergence, while student phases I and II are each trained for 10 epochs. We use Adam optimizer with momentum terms (0.9, 0.999). For fair comparison with prior work (He et al., 2023), we adopt the same configuration of transformer blocks, attention heads, and channel dimensions: [3, 3, 3, 3], [1, 2, 4, 8], and [64, 128, 256, 512] from levels 1-4. During inference, we make 4 function evaluation calls for rectified flow generation, yielding faster generation and higher-quality outputs compared to state-of-the-art methods. Training follows the methodology of Reti-Diff and CIDNet across datasets and tasks.

Quantitative Evaluation. For the low-light image enhancement (LLIE) task, we conduct experiments on LOL-v1 (Wei et al., 2018), LOL-v2-real, LOL-v2-syn (Yang et al., 2021), and SID (Chen et al., 2019). Performance is evaluated with PSNR, SSIM, FID, and BIQI (Hore & Ziou, 2010; Moorthy & Bovik, 2010), where higher PSNR/SSIM and lower FID/BIQI indicate better results. RestoRect achieves state-of-the-art performance across all datasets shown in Table 2, with improvements on almost every metric over the second-best methods (RetiDiff and CIDNet). The visual results shown in Figure 4 highlight clear improvements in fine grained details shown in cyan boxes (please zoom in for clarity).

For the underwater image enhancement (UIE) task, we evaluate on UIEB (Li et al., 2019) and LSUI (Peng et al., 2023), using PSNR, SSIM, and UIQM (Panetta et al., 2015). Higher values across all metrics indicate better performance. RestoRect outperforms RetiDiff by 1.76dB PSNR on UIEB and matches its performance on LSUI while achieving superior SSIM scores shown in Table 3. For the backlit image enhancement (BAID) task, experiments are performed (Lv et al., 2022), with evaluation on PSNR, SSIM, and FID. RestoRect demonstrates substantial improvements with 4.48dB PSNR gain over RetiDiff and 11.65 FID reduction shown in Table 4. Additionally, we test on real-world fundus image enhancement (FIE) (Shen et al., 2020) images using the LOL-v2-syn pretrained model, evaluating with BIQI and CLIPIQA (Wang et al., 2023b), where higher CLIPIQA values indicate better performance. RestoRect achieves the lowest BIQI score of 6.033, outperforming SNRNet shown in Table 5. The visual results shown in Figure 5 highlight our performance with details shown in yellow boxes (please zoom in for clarity). We note that Reti-Diff baseline images for UIEB and LSUI in middle row very closely match the ground truth while the scores are marginally worse than ours. This makes us believe that the publicly available checkpoints provided on Reti-Diff's github might be overfitted to the validation set, unlike our model which has not seen the validation set.

For real-world image restoration, we test on five unpaired datasets: DCIM (Lee et al., 2013), LIME (Guo et al., 2016), MEF (Wang et al., 2013), NPE (Ma et al., 2015), and VV (He et al., 2025a). Using the LOL-v2-syn pretrained model for inference, we evaluate with BRISQUE (Mittal et al., 2012), where lower values are better. RestoRect consistently outperforms CIDNet across most datasets, achieving the best scores on DCIM (16.56), LIME (16.12), and VV (24.42) as shown in Table 6. We further evaluate on single image contrast enhancement (SICE) (Cai et al., 2018), which contains underexposed and overexposed images, training on the resized SICE training set and test on the datasets SICE-Mix and SICE-Grad (Zheng et al., 2022) with metrics PSNR, SSIM, LPIPS.

Table 2: LLIE task results. Best result shown in Green and second best shown in Blue. We also include our performance on RestoRect reconstruction teacher model.

Methods	LOL-v1				LOL-v2-real				LOL-v2-syn				SID			
	PSNR↑	SSIM↑	FID↓	BIQI↓	PSNR↑	SSIM↑	FID↓	BIQI↓	PSNR↑	SSIM↑	FID↓	BIQI↓	PSNR↑	SSIM↑	FID↓	BIQI↓
MRQ (Liu et al., 2023)	25.24	0.855	53.32	22.73	22.37	0.854	68.89	33.61	25.54	0.940	21.56	25.09	24.80	0.688	63.72	29.53
IAGC (Wang et al., 2023c)	24.53	0.866	59.73	25.50	22.20	0.863	70.34	31.70	25.58	0.941	21.58	30.32	23.17	0.640	78.80	30.56
DiffIR (Xia et al., 2023)	23.15	0.828	70.13	26.38	21.15	0.816	72.33	29.15	24.76	0.921	21.36	27.74	23.17	0.640	78.80	30.56
CUE (Zheng et al., 2023)	21.86	0.841	69.83	27.15	21.19	0.829	67.05	28.83	24.41	0.917	31.34	33.83	23.25	0.652	77.38	28.85
GSAD (Hou et al., 2023)	20.33	0.852	51.64	19.96	20.90	0.847	46.77	28.85	24.22	0.927	19.24	25.76	–	–	–	–
AST (Zhou et al., 2024)	21.09	0.858	87.67	21.23	21.68	0.857	91.81	25.17	22.25	0.927	19.20	20.78	–	–	–	–
Mamba (Guo et al., 2024)	22.33	0.863	63.39	20.17	21.97	0.840	56.09	24.46	25.75	**0.958**	17.95	20.37	21.14	0.656	154.76	32.72
RetiDiff (He et al., 2023)	**25.35**	0.866	49.14	17.75	22.97	0.858	**43.18**	23.66	**27.53**	0.951	**13.82**	**15.77**	**25.53**	**0.692**	**51.66**	**25.58**
CIDNet (Yan et al., 2024)	23.50	**0.900**	**46.69**	**14.77**	**24.11**	**0.871**	48.04	**18.45**	25.71	0.942	18.60	15.87	22.90	0.676	55.29	29.12
RestoRect (teacher only)	22.18	0.862	63.77	26.50	20.11	0.833	65.84	29.21	23.15	0.911	28.72	28.13	22.60	0.717	68.42	27.13
RestoRect	**27.84**	**0.945**	**38.67**	**8.35**	**22.97**	**0.911**	**42.80**	**10.47**	**27.69**	**0.968**	**16.75**	**11.67**	**26.19**	**0.923**	**54.23**	**19.57**

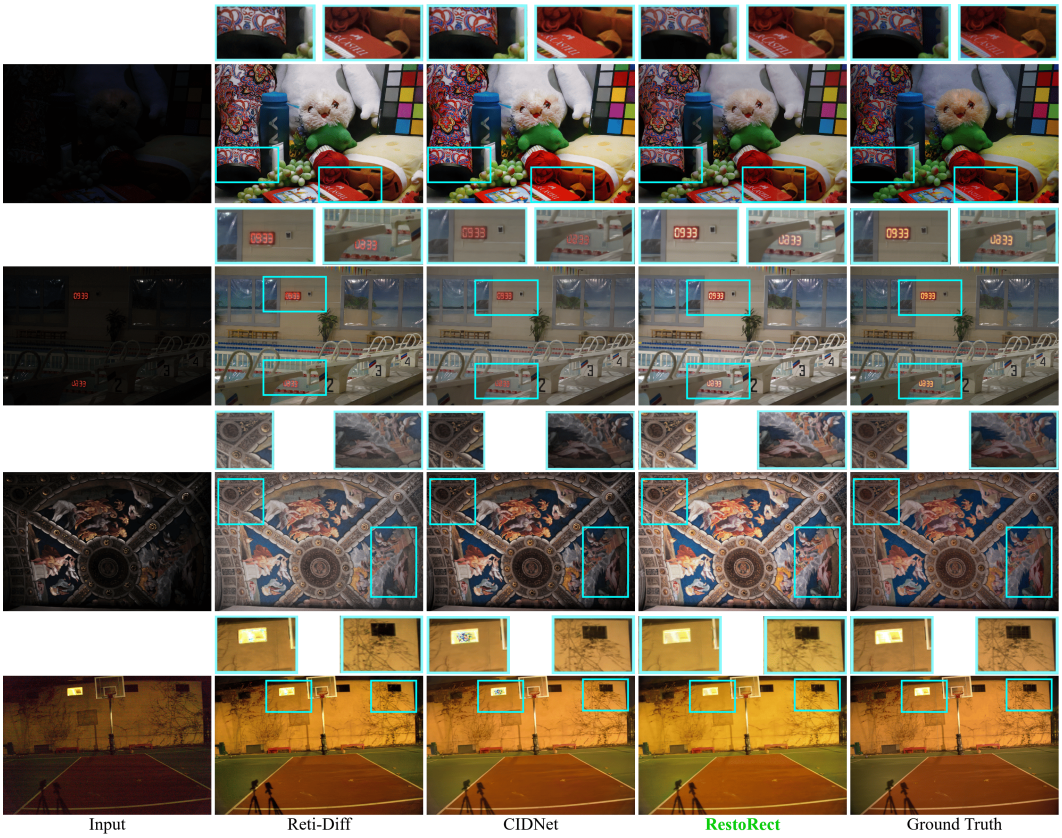

Figure 4: LLIE task visual results (Top to Bottom: LOL-v1, v2-real, v2-syn, SID). Clear improvements in fine grained details are shown in cyan boxes (please zoom in for clarity).

RestoRect achieves superior PSNR and SSIM performance over CIDNet by 1.6dB and 0.031 on SICE-Mix, and 2.0dB and 0.077 on SICE-Grad, as shown in Table 7.

Qualitative Evaluation. We conduct a user study to evaluate low-light image enhancement. Eight participants are shown 20 low-light images alongside enhanced outputs from RestoRect, Reti-Diff, and CIDNet (RAVE included for BAID dataset). In a blind comparison, subjects are asked to select the result that appears closest to the ground truth. Figure 8 presents the preference distributions, showing that RestoRect consistently achieves the highest preference across all five datasets, highlighting its ability to generate visually appealing results perceived as closest to the ground truth. Figure 8 and Table 11 shows comparison of RestoRect's student model parameter size (M) and GFLOPs against other transformer architecture baselines demonstrating efficiency.

Table 3: UIE task results

Methods	UIEB			LSUI		
	PSNR↑	SSIM↑	UIQM↑	PSNR↑	SSIM↑	UIQM↑
SUnwet (Naik et al., 2021)	18.28	0.855	2.942	20.89	0.875	2.746
PUIE (Fu et al., 2022)	21.38	0.882	3.021	23.70	0.902	2.974
UShape (Peng et al., 2023)	22.91	0.905	2.896	24.16	0.917	3.022
PUGAN (Cong et al., 2023)	23.05	0.897	2.902	25.06	0.916	3.106
ADP (Zhou et al., 2023)	22.90	0.892	3.005	24.28	0.913	3.075
NU2Net (Guo et al., 2023)	22.38	0.903	2.936	25.07	0.908	3.112
AST (Zhou et al., 2024)	22.19	0.908	2.981	27.46	0.916	3.107
Mamba (Guo et al., 2024)	22.60	**0.939**	2.991	27.68	0.916	3.118
RetiDiff (He et al., 2023)	**24.12**	0.910	**3.088**	**28.10**	**0.929**	**3.208**
RestoRect	**25.88**	**0.950**	**3.121**	**28.10**	**0.937**	**3.229**

Table 4: BAID task results

Methods	BAID		
	PSNR↑	SSIM↑	FID↓
EnGAN (Jiang et al., 2021)	17.96	0.819	43.55
URetinex (Wu et al., 2022)	19.08	0.845	42.26
CLIPLIT (Liang et al., 2023)	21.13	0.853	37.30
DiffRet (Yi et al., 2023)	22.07	0.861	38.07
DiffIR (Xia et al., 2023)	21.10	0.835	40.35
AST (Zhou et al., 2024)	22.61	0.851	32.47
Mamba (Guo et al., 2024)	23.07	0.874	29.13
RAVE (Gaintseva et al., 2024)	21.26	0.872	64.89
RetiDiff (He et al., 2023)	**23.19**	**0.876**	**27.47**
RestoRect	**27.67**	**0.965**	**15.82**

Table 5: FIE task results

Methods	Fundus	
	BIQI↓	CLIPQ↑
SNRNet (Xu et al., 2022)	**6.144**	**0.557**
URetinex (Wu et al., 2022)	12.158	**0.561**
SCI (Ma et al., 2022)	23.527	0.552
MIRNet (Zamir et al., 2022)	14.925	0.527
FourLLE (Wang et al., 2023a)	7.741	0.508
CUE (Zheng et al., 2023)	11.721	0.448
NeRCO (Yang et al., 2023)	17.256	0.451
RetiDiff (He et al., 2023)	10.788	0.525
CIDNet (Yan et al., 2024)	10.663	0.529
RestoRect	**6.033**	0.503

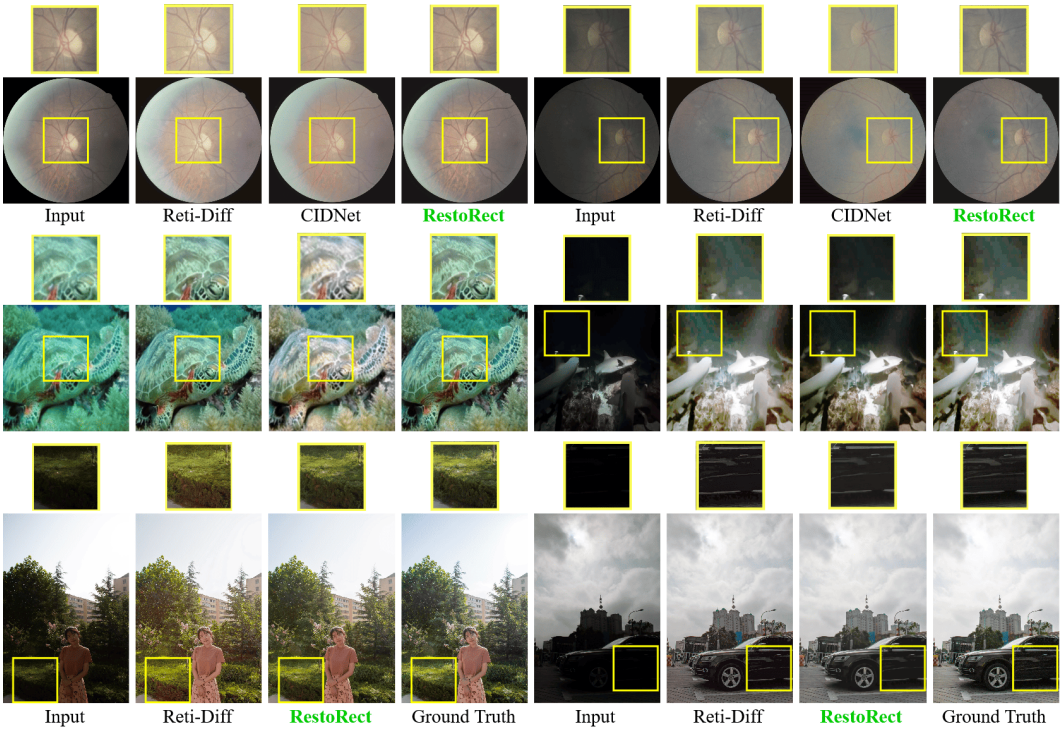

Figure 5: FIE (Top), UIEB (Middle Left), LSUI (Middle Right), BAID (Bottom) task visual results. Clear improvements in fine grained details are shown in yellow boxes (please zoom in for clarity).

Ablation and Generalizability. Figure 3 presents the results of teacher model training under different ablation settings. The removal of auxiliary constraints, such as anisotropic diffusion and the polarized HVI color space loss, is shown in blue. In contrast, the ablation of SCLN and QK normalization from the transformer block is shown in red, where a standard layer normalization and vanilla QK computation are used instead, following (He et al., 2023). As illustrated in green, the teacher model achieves the best performance with RestoRect when all proposed components are included. Table 8 further reports student model performance across different training and testing conditions on the LOL-v1, LOL-v2-real, and LOL-v2-synthetic datasets. In the table, '-FLEX' denotes models trained on the same dataset as the test set but without the FLEX loss. The FLEX training strategy demonstrates substantial improvements, with gains across all metrics compared to the full model results shown in Table 2. Subsequent rows in Table 8 evaluate cross-dataset transfer, where models trained on one dataset are tested on another, highlighting their strong generalization capacity. These results demonstrate that models trained for a given task can effectively transfer knowledge and serve as strong initialization points for fine-tuning on other datasets. Figure 7 shows visual results for LLIE task with ablation of SCLN and QK Norm, Auxiliary constraints, FLEX loss, compared to full RestoRect architecture and Ground Truth. Figure 3 also demonstrates the FID performance of RestoRect across different inference steps for the LLIE task. Our rectified flow formulation consistently outperforms (He et al., 2023) DDIM across all LLIE datasets, generating restored image within 3-4 steps, making it ideal for real time applications.

Table 6: Unpaired task results

Methods	DCIM	LIME	MEF	NPE	VV
	BRISQUE↓				
KinD (Zhang et al., 2019)	48.72	39.91	49.94	36.85	50.56
ZeroDCE (Guo et al., 2020)	27.56	20.44	17.32	24.72	34.66
RUAS (Liu et al., 2021)	38.75	27.59	23.68	47.85	38.37
LLFlow (Wang et al., 2022)	26.36	27.06	30.27	28.86	31.67
SNRAware (Xu et al., 2022)	37.35	39.22	31.28	26.65	78.72
PairLIE (Fu et al., 2023)	33.31	25.23	27.53	28.27	39.13
CIDNet (Yan et al., 2024)	**21.47**	**16.25**	**13.77**	**18.92**	**30.63**
RestoRect	**16.56**	**16.12**	**14.69**	**23.91**	**24.42**

Table 7: SICE task results

Methods	SICE-Mix			SICE-Grad		
	PSNR↑	SSIM↑	LPIPS↓	PSNR↑	SSIM↑	LPIPS↓
RetiNet (Wei et al., 2018)	12.397	0.606	0.407	12.450	0.619	0.364
ZeroDCE (Guo et al., 2020)	12.428	0.633	**0.382**	12.475	0.644	**0.334**
URetinex (Wu et al., 2022)	10.903	0.600	0.402	10.894	0.610	0.356
RUAS (Liu et al., 2021)	8.684	0.493	0.525	8.628	0.494	0.499
LLFlow (Wang et al., 2022)	12.737	0.617	0.388	12.737	0.617	0.388
LEDNet (Zhou et al., 2022)	12.668	0.579	0.412	12.551	0.576	0.383
CIDNet (Yan et al., 2024)	**13.425**	**0.636**	**0.362**	**13.446**	**0.648**	**0.318**
RestoRect	**15.041**	**0.667**	0.393	**15.447**	**0.715**	0.354

Table 8: Ablation

Test	Train	PSNR↑	SSIM↑	FID↓	BIQI↓
v1	-FLEX	24.27	0.891	44.75	9.02
	v2-s	18.32	0.827	99.36	18.74
	v2-r	17.57	0.827	111.66	21.68
v2-r	-FLEX	23.16	0.880	41.55	10.52
	v1	22.27	0.874	48.92	18.57
	v2-s	21.15	0.837	106.29	22.92
v2-s	-FLEX	27.89	0.942	17.93	11.95
	v1	19.96	0.876	69.37	16.39
	v2-r	17.18	0.768	117.84	25.26

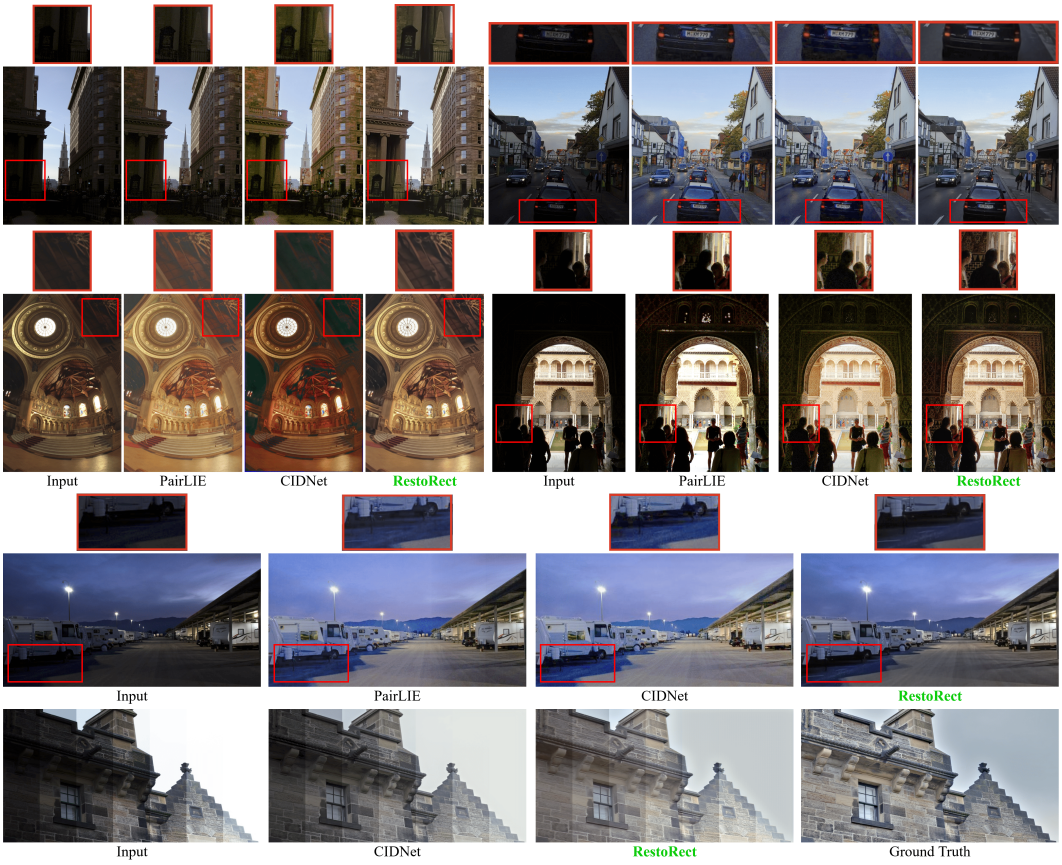

Figure 6: DCIM (Row 1 Left), LIME (Row 1 Right), MEF (Row 2 Left), NPE (Row 2 Right), VV (Row 3), SICE-Grad (Row 4) task visual results. Clear improvements in fine grained details are shown in red boxes (please zoom in for clarity).

The student model ablation study on LOL-v1 dataset in Table 9 evaluates the contribution of each component in the knowledge distillation framework. The metrics demonstrate that the combination of Rectified Flow (RF) with Trajectory Consistency (RF+TC) and FLEX loss components yields substantial improvements over traditional KD methods of (He et al., 2023), with the full configuration achieving 27.84 PSNR, 0.945 SSIM, 38.67 FID, and 8.35 BIQI on LOL-v1. The incremental addition of FLEX components shows that Cross-Normalization (CN) alone provides modest gains, while adding Percentile Masking (PM) delivers significant improvements (27.82 PSNR), and the complete FLEX formulation with Resolution Weighting (RW) achieves optimal performance. Hyperparameter analysis reveals that the percentile threshold of 95% for outlier detection and SNR threshold of 0.4 provide the best balance between training stability and performance.

Failure Cases. Despite strong performance across many restoration tasks, RestoRect is limitated in extreme degradation scenarios seen in Figure 9. Failure occurs when input images contain severe overexposure or underexposure with complete information loss in large spatial regions. The model produces unrealistic artifacts including color bleeding, checkerboard-like noise patterns, and hallucinatory textures that deviate from natural image statistics. These artifacts are highlighted in the

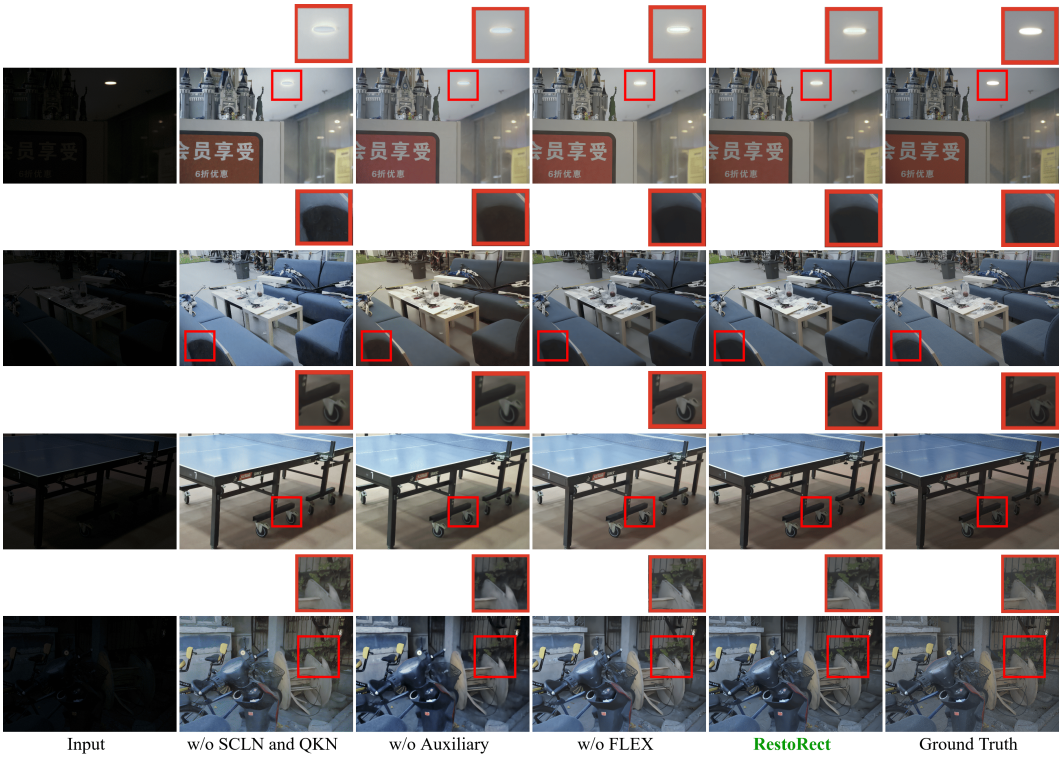

Figure 7: LLIE task visual results with ablation of SCLN and QK Norm, Auxiliary constraints, FLEX loss, compared to full RestoRect model and Ground Truth.

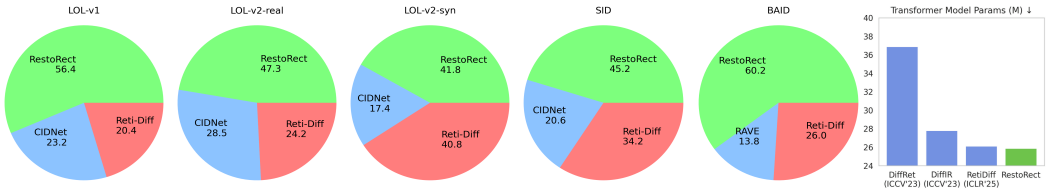

Figure 8: Qualitative human evaluation user study on LLIE and BAID datasets. Student model parameter size (M) comparison against other transformer architecture baselines showing efficiency.

zoomed regions in red boxes, where recovered areas show synthetic-looking patterns rather than coherent scene content. These cases reveal that when the signal-to-noise ratio falls below a threshold, velocity prediction networks struggle to generate meaningful features, resulting in the model relying on learned priors that introduce perceptually implausible reconstructions.

Table 9: Student ablation study (L-v1).

Configuration	PSNR↑	SSIM↑	FID↓	BIQI↓
RetiDiff (Traditional KD)	25.35	0.866	49.14	17.75
RF(no TC) + no FLEX	24.10	0.855	49.28	17.95
RF(TC) + no FLEX	24.27	0.891	44.75	9.02
RF(TC) + FLEX(CN)	25.64	0.913	42.18	8.73
RF(TC) + FLEX(CN+PM)	27.82	**0.947**	39.25	8.42
RF(TC) + FLEX(CN+PM+RW)	**27.84**	0.945	**38.67**	**8.35**
Percentile Threshold $p = 85\%$	26.21	0.898	39.84	8.58
Percentile Threshold $p = 90\%$	27.58	**0.946**	39.12	8.43
Percentile Threshold $p = 95\%$	**27.84**	0.945	**38.67**	**8.35**
Percentile Threshold $p = 99\%$	27.67	0.943	38.91	8.41
SNR Threshold $\tau_{SNR} = 0.2$	27.15	0.937	40.12	8.64
SNR Threshold $\tau_{SNR} = 0.4$	27.84	**0.945**	**38.67**	**8.35**
SNR Threshold $\tau_{SNR} = 0.6$	**27.89**	0.941	39.28	8.47
SNR Threshold $\tau_{SNR} = 0.8$	26.92	0.934	40.53	8.71

Figure 9: Failure cases on SICE-Mix dataset.

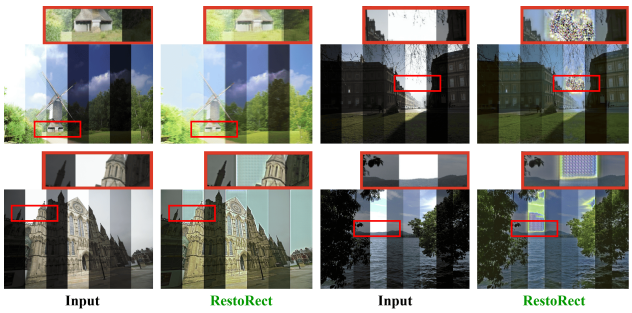

Downstream Application. For downstream application, RestoRect demonstrates strong transfer capability on the ExDark (Loh & Chan, 2019) low-light object detection task shown in Table 10. Following (Cai et al., 2023) and (He et al., 2023), low light images from the ExDark dataset were restored and object-detection task was performed using YOLOv3 model. Images enhanced by RestoRect achieve 77.1% mean average precision across 12 object categories, outperforming RetiDiff (He et al., 2023) (75.8%) and other methods. Improvements are observed in categories like Bicycle (85.8%), Bottle (79.5%), and Motor (77.9%), indicating that the restoration quality translates to real-world vision tasks.

Table 10: Downstream application on low-light image detection task on ExDark dataset.

Methods	Bicycle	Boat	Bottle	Bus	Car	Cat	Chair	Cup	Dog	Motor	People	Table	Mean
Restormer	77.0	71.0	68.8	91.6	77.1	62.5	57.3	68.0	69.6	69.2	74.6	49.7	69.7
SCI	73.4	68.0	69.5	86.2	74.5	63.1	59.5	61.0	67.3	63.9	73.2	47.3	67.2
SNR-Net	78.3	74.2	74.5	89.6	82.7	66.8	66.3	62.5	74.7	63.1	73.3	57.2	71.9
Retformer	78.1	74.5	74.2	91.2	82.2	65.0	63.3	67.0	75.4	68.6	75.3	55.6	72.5
RetiDiff	**82.0**	**77.9**	**76.4**	**92.2**	**83.3**	**69.6**	**67.4**	**74.4**	**75.5**	**74.3**	**78.3**	**57.9**	**75.8**
RestoRect	**85.8**	**79.1**	**79.5**	**91.5**	**83.5**	**70.2**	**68.8**	**74.1**	**78.2**	**77.9**	**78.2**	**57.4**	**77.1**

Table 11: Transformer model complexity comparison

Methods	Source	Params M	GFLOPs
Restormer	CVPR'22	26.13	144.25
Diff-Reti	ICCV'23	56.88	198.16
DiffIR	ICCV'23	27.80	35.32
GSAD	NIPS'23	17.17	670.33
Reti-Diff	ICLR'25	26.11	87.63
RestoRect	Ours	25.87	49.50

Table 12: RestoRect Image Quality Evaluation Results for all 15 datasets across 10 metrics

Dataset	PSNR	SSIM	FID	NIQE	LPIPS	BRISQ	BIQI	UCIQE	UIQM	CLIPQ
LOL-v1	27.85	0.94	38.67	7.47	0.11	27.16	8.35	0.52	2.60	0.499
LOL-v2 Real	22.97	0.91	42.81	7.74	0.13	28.44	10.48	**0.51**	2.88	0.500
LOL-v2 Syn	27.70	0.97	16.75	5.74	0.06	15.68	11.68	0.55	2.77	0.498
SID	26.19	0.92	54.23	5.87	0.15	20.05	**19.57**	0.85	2.38	0.498
UIEB	25.89	0.95	20.26	6.49	0.11	17.89	13.99	0.58	3.12	0.501
LSUI	28.10	0.94	17.83	5.04	0.18	21.82	16.06	0.57	3.23	0.499
BAID	27.68	0.97	15.83	8.11	0.06	**34.39**	10.49	0.56	2.87	0.501
Fundus	20.45	0.92	37.04	**8.27**	0.06	27.54	6.03	0.60	**2.06**	0.503
DCIM	19.92	0.82	72.72	6.36	0.17	16.57	10.26	0.57	2.33	0.499
LIME	18.36	0.76	101.31	6.12	0.21	16.13	11.76	0.59	2.19	0.497
MEF	17.20	0.69	74.06	6.13	0.26	14.70	11.23	0.56	2.83	0.499
NPE	16.28	0.77	63.75	7.10	0.18	23.91	12.91	0.53	2.64	0.498
VV	17.45	0.80	91.08	7.55	0.20	24.42	9.81	0.63	2.20	0.498
SICE (mix)	**15.04**	**0.67**	**125.23**	6.60	**0.39**	21.88	11.51	0.54	3.02	**0.496**
SICE (grad)	15.45	0.72	80.86	6.32	0.35	21.98	11.16	0.54	2.95	0.497

5 Conclusion

We present RestoRect, a generative knowledge distillation framework that reformulates degraded image restoration through latent rectified flow. Unlike traditional approaches that rely on static feature matching, RestoRect models feature transfer through learnable trajectories and introduces the FLEX loss for principled distribution alignment. Combined with a specialized U-Net transformer architecture and physics-based constraints, our method achieves state-of-the-art results across 15 datasets covering low-light, underwater, backlit, and fundus enhancement. RestoRect delivers better perceptual quality with only 4 inference steps, making it both effective and computationally efficient. Beyond restoration, this generative distillation method highlights new opportunities for efficient model compression and cross-architecture transfer in computer vision, establishing potential foundation for broader advances in fast high-quality image, and video restoration for future work.

6 List of Acronyms

Table 13: List of acronyms used in this paper

Acronym	Full Form
Tasks & Methods	
LLIE	Low-Light Image Enhancement
UIE	Underwater Image Enhancement
FIE	Fundus Image Enhancement
SCLN	Spatial Channel Layer Normalization
FLEX	Feature Layer EXtraction Loss
Datasets	
LOL	Low-light Outdoor Lighting
SID	See in the Dark
UIEB	Underwater Image Enhancement Bench
LSUI	Large Scale Underwater Image
BAID	Backlit Image Dataset
DCIM	Digital Camera Image
LIME	Low-light Image Enhancement
MEF	Multi-Exposure Fusion
NPE	Naturalness Preserved Enhancement
VV	Video Visibility
SICE	Single Image Contrast Enhancement

Acronym	Full Form
Evaluation Metrics	
PSNR	Peak Signal-to-Noise Ratio
SSIM	Structural Similarity Index Measure
FID	Fréchet Inception Distance
NIQE	Natural Image Quality Evaluator
LPIPS	Learned Perceptual Image Patch Similarity
BRISQUE	Blind/Referenceless Image Spatial Quality Evaluator
BIQI	Blind Image Quality Index
UCIQE	Underwater Color Image Quality Evaluation
UIQM	Underwater Image Quality Measure
CLIPIQA	CLIP-based Image Quality Assessment
Other Technical Terms	
HVI	Horizontal-Vertical-Intensity
VGG	Visual Geometry Group
ODE	Ordinary Differential Equation
DDIM	Denoising Diffusion Implicit Model
QK	Query-Key
GT / LQ	Ground Truth / Low Quality

REFERENCES

Tariq Berrada, Pietro Astolfi, Melissa Hall, Marton Havasi, Yohann Benchetrit, Adriana Romero-Soriano, Karteek Alahari, Michal Drozdzal, and Jakob Verbeek. Boosting latent diffusion with perceptual objectives. In *The Thirteenth International Conference on Learning Representations*, 2025.

Zhaodong Bing, Linze Li, and Jiajun Liang. Optimizing knowledge distillation in transformers: Enabling multi-head attention without alignment barriers. *arXiv preprint arXiv:2502.07436*, 2025.

Jianrui Cai, Shuhang Gu, and Lei Zhang. Learning a deep single image contrast enhancer from multi-exposure images. *IEEE Transactions on Image Processing*, 27(4):2049–2062, 2018.

Yuanhao Cai, Hao Bian, Jing Lin, Haoqian Wang, Radu Timofte, and Yulun Zhang. Retinexformer: One-stage retinex-based transformer for low-light image enhancement. In *Proceedings of the IEEE/CVF international conference on computer vision*, pp. 12504–12513, 2023.

Hu Cao, Yueyue Wang, Joy Chen, Dongsheng Jiang, Xiaopeng Zhang, Qi Tian, and Manning Wang. Swin-unet: Unet-like pure transformer for medical image segmentation. In *European conference on computer vision*, pp. 205–218. Springer, 2022.

Chen Chen, Qifeng Chen, Minh N Do, and Vladlen Koltun. Seeing motion in the dark. In *Proceedings of the IEEE/CVF International conference on computer vision*, pp. 3185–3194, 2019.

Heng-Da Cheng and XJ Shi. A simple and effective histogram equalization approach to image enhancement. *Digital signal processing*, 14(2):158–170, 2004.

Runmin Cong, Wenyu Yang, Wei Zhang, Chongyi Li, Chun-Le Guo, Qingming Huang, and Sam Kwong. Pugan: Physical model-guided underwater image enhancement using gan with dual-discriminators. *IEEE Transactions on Image Processing*, 32:4472–4485, 2023.

Land Edwin. The retinex theory of color vision. *Scientific american*, 237:108–128, 1977.

Xueyang Fu, Delu Zeng, Yue Huang, Xiao-Ping Zhang, and Xinghao Ding. A weighted variational model for simultaneous reflectance and illumination estimation. In *Proceedings of the IEEE conference on computer vision and pattern recognition*, pp. 2782–2790, 2016.

Zhenqi Fu, Wu Wang, Yue Huang, Xinghao Ding, and Kai-Kuang Ma. Uncertainty inspired underwater image enhancement. In *European conference on computer vision*, pp. 465–482. Springer, 2022.

Zhenqi Fu, Yan Yang, Xiaotong Tu, Yue Huang, Xinghao Ding, and Kai-Kuang Ma. Learning a simple low-light image enhancer from paired low-light instances. In *Proceedings of the IEEE/CVF conference on computer vision and pattern recognition*, pp. 22252–22261, 2023.

Tatiana Gaintseva, Martin Benning, and Gregory Slabaugh. Rave: Residual vector embedding for clip-guided backlit image enhancement. In *European Conference on Computer Vision*, pp. 412–428. Springer, 2024.

Chunle Guo, Chongyi Li, Jichang Guo, Chen Change Loy, Junhui Hou, Sam Kwong, and Runmin Cong. Zero-reference deep curve estimation for low-light image enhancement. In *Proceedings of the IEEE/CVF conference on computer vision and pattern recognition*, pp. 1780–1789, 2020.

Chunle Guo, Ruiqi Wu, Xin Jin, Linghao Han, Weidong Zhang, Zhi Chai, and Chongyi Li. Underwater ranker: Learn which is better and how to be better. In *Proceedings of the AAAI conference on artificial intelligence*, volume 37, pp. 702–709, 2023.

Hang Guo, Jinmin Li, Tao Dai, Zhihao Ouyang, Xudong Ren, and Shu-Tao Xia. Mambair: A simple baseline for image restoration with state-space model. In *European conference on computer vision*, pp. 222–241. Springer, 2024.

Xiaojie Guo, Yu Li, and Haibin Ling. Lime: Low-light image enhancement via illumination map estimation. *IEEE Transactions on image processing*, 26(2):982–993, 2016.

Chunming He, Chengyu Fang, Yulun Zhang, Tian Ye, Kai Li, Longxiang Tang, Zhenhua Guo, Xiu Li, and Sina Farsiu. Reti-diff: Illumination degradation image restoration with retinex-based latent diffusion model. *arXiv preprint arXiv:2311.11638*, 2023.

Chunming He, Yuqi Shen, Chengyu Fang, Fengyang Xiao, Longxiang Tang, Yulun Zhang, Wangmeng Zuo, Zhenhua Guo, and Xiu Li. Diffusion models in low-level vision: A survey. *IEEE Transactions on Pattern Analysis and Machine Intelligence*, 2025a.

Chunming He, Rihan Zhang, Fengyang Xiao, Chengyu Fang, Longxiang Tang, Yulun Zhang, and Sina Farsiu. Unfoldir: Rethinking deep unfolding network in illumination degradation image restoration. *arXiv preprint arXiv:2505.06683*, 2025b.

Byeongho Heo, Jeesoo Kim, Sangdoo Yun, Hyojin Park, Nojun Kwak, and Jin Young Choi. A comprehensive overhaul of feature distillation. In *Proceedings of the IEEE/CVF international conference on computer vision*, pp. 1921–1930, 2019.

Geoffrey Hinton, Oriol Vinyals, and Jeff Dean. Distilling the knowledge in a neural network. *arXiv preprint arXiv:1503.02531*, 2015.

Jonathan Ho, William Chan, Chitwan Saharia, Jay Whang, Ruiqi Gao, Alexey Gritsenko, Diederik P Kingma, Ben Poole, Mohammad Norouzi, David J Fleet, et al. Imagen video: High definition video generation with diffusion models. *arXiv preprint arXiv:2210.02303*, 2022.

Alain Hore and Djemel Ziou. Image quality metrics: Psnr vs. ssim. In *2010 20th international conference on pattern recognition*, pp. 2366–2369. IEEE, 2010.

Jinhui Hou, Zhiyu Zhu, Junhui Hou, Hui Liu, Huanqiang Zeng, and Hui Yuan. Global structure-aware diffusion process for low-light image enhancement. *Advances in Neural Information Processing Systems*, 36:79734–79747, 2023.

Huimin Huang, Lanfen Lin, Ruofeng Tong, Hongjie Hu, Qiaowei Zhang, Yutaro Iwamoto, Xianhua Han, Yen-Wei Chen, and Jian Wu. Unet 3+: A full-scale connected unet for medical image segmentation. In *ICASSP 2020-2020 IEEE international conference on acoustics, speech and signal processing (ICASSP)*, pp. 1055–1059. Ieee, 2020.

Shih-Chia Huang, Fan-Chieh Cheng, and Yi-Sheng Chiu. Efficient contrast enhancement using adaptive gamma correction with weighting distribution. *IEEE transactions on image processing*, 22(3):1032–1041, 2012.

Zehao Huang and Naiyan Wang. Like what you like: Knowledge distill via neuron selectivity transfer. *arXiv preprint arXiv:1707.01219*, 2017.

Yifan Jiang, Xinyu Gong, Ding Liu, Yu Cheng, Chen Fang, Xiaohui Shen, Jianchao Yang, Pan Zhou, and Zhangyang Wang. Enlightengan: Deep light enhancement without paired supervision. *IEEE transactions on image processing*, 30:2340–2349, 2021.

Xiaoqi Jiao, Yichun Yin, Lifeng Shang, Xin Jiang, Xiao Chen, Linlin Li, Fang Wang, and Qun Liu. Tinybert: Distilling bert for natural language understanding. *arXiv preprint arXiv:1909.10351*, 2019.

Durk P Kingma and Prafulla Dhariwal. Glow: Generative flow with invertible 1x1 convolutions. *Advances in neural information processing systems*, 31, 2018.

Chulwoo Lee, Chul Lee, and Chang-Su Kim. Contrast enhancement based on layered difference representation of 2d histograms. *IEEE transactions on image processing*, 22(12):5372–5384, 2013.

Chongyi Li, Chunle Guo, Wenqi Ren, Runmin Cong, Junhui Hou, Sam Kwong, and Dacheng Tao. An underwater image enhancement benchmark dataset and beyond. *IEEE transactions on image processing*, 29:4376–4389, 2019.

Mading Li, Jiaying Liu, Wenhan Yang, Xiaoyan Sun, and Zongming Guo. Structure-revealing low-light image enhancement via robust retinex model. *IEEE transactions on image processing*, 27 (6):2828–2841, 2018.

Zhexin Liang, Chongyi Li, Shangchen Zhou, Ruicheng Feng, and Chen Change Loy. Iterative prompt learning for unsupervised backlit image enhancement. In *Proceedings of the IEEE/CVF International Conference on Computer Vision*, pp. 8094–8103, 2023.

Sihao Lin, Hongwei Xie, Bing Wang, Kaicheng Yu, Xiaojun Chang, Xiaodan Liang, and Gang Wang. Knowledge distillation via the target-aware transformer. In *Proceedings of the IEEE/CVF conference on computer vision and pattern recognition*, pp. 10915–10924, 2022.

Risheng Liu, Long Ma, Jiaao Zhang, Xin Fan, and Zhongxuan Luo. Retinex-inspired unrolling with cooperative prior architecture search for low-light image enhancement. In *Proceedings of the IEEE/CVF conference on computer vision and pattern recognition*, pp. 10561–10570, 2021.

Xingchao Liu, Chengyue Gong, and Qiang Liu. Flow straight and fast: Learning to generate and transfer data with rectified flow. *arXiv preprint arXiv:2209.03003*, 2022.

Yunlong Liu, Tao Huang, Weisheng Dong, Fangfang Wu, Xin Li, and Guangming Shi. Low-light image enhancement with multi-stage residue quantization and brightness-aware attention. In *Proceedings of the IEEE/CVF International Conference on Computer Vision*, pp. 12140–12149, 2023.

Yuen Peng Loh and Chee Seng Chan. Getting to know low-light images with the exclusively dark dataset. *Computer vision and image understanding*, 178:30–42, 2019.

Xiaoqian Lv, Shengping Zhang, Qinglin Liu, Haozhe Xie, Bineng Zhong, and Huiyu Zhou. Backlitnet: A dataset and network for backlit image enhancement. *Computer Vision and Image Understanding*, 218:103403, 2022.

Kede Ma, Kai Zeng, and Zhou Wang. Perceptual quality assessment for multi-exposure image fusion. *IEEE Transactions on Image Processing*, 24(11):3345–3356, 2015.

Long Ma, Tengyu Ma, Risheng Liu, Xin Fan, and Zhongxuan Luo. Toward fast, flexible, and robust low-light image enhancement. In *Proceedings of the IEEE/CVF conference on computer vision and pattern recognition*, pp. 5637–5646, 2022.

Anish Mittal, Anush Krishna Moorthy, and Alan Conrad Bovik. No-reference image quality assessment in the spatial domain. *IEEE Transactions on image processing*, 21(12):4695–4708, 2012.

Anush Krishna Moorthy and Alan Conrad Bovik. A two-step framework for constructing blind image quality indices. *IEEE Signal processing letters*, 17(5):513–516, 2010.

Ankita Naik, Apurva Swarnakar, and Kartik Mittal. Shallow-uwnet: Compressed model for underwater image enhancement (student abstract). In *Proceedings of the AAAI Conference on Artificial Intelligence*, volume 35, pp. 15853–15854, 2021.

Karen Panetta, Chen Gao, and Sos Agaian. Human-visual-system-inspired underwater image quality measures. *IEEE Journal of Oceanic Engineering*, 41(3):541–551, 2015.

Lintao Peng, Chunli Zhu, and Liheng Bian. U-shape transformer for underwater image enhancement. *IEEE transactions on image processing*, 32:3066–3079, 2023.

Pietro Perona, Takahiro Shiota, and Jitendra Malik. Anisotropic diffusion. In *Geometry-driven diffusion in computer vision*, pp. 73–92. Springer, 1994.

Adriana Romero, Nicolas Ballas, Samira Ebrahimi Kahou, Antoine Chassang, Carlo Gatta, and Yoshua Bengio. Fitnets: Hints for thin deep nets. arxiv 2014. *arXiv preprint arXiv:1412.6550*, 2014.

Chitwan Saharia, William Chan, Huiwen Chang, Chris Lee, Jonathan Ho, Tim Salimans, David Fleet, and Mohammad Norouzi. Palette: Image-to-image diffusion models. In *ACM SIGGRAPH 2022 conference proceedings*, pp. 1–10, 2022.

Ziyi Shen, Huazhu Fu, Jianbing Shen, and Ling Shao. Modeling and enhancing low-quality retinal fundus images. *IEEE Transactions on Medical Imaging*, 40(3):996–1006, 2020.

Karen Simonyan and Andrew Zisserman. Very deep convolutional networks for large-scale image recognition. *arXiv preprint arXiv:1409.1556*, 2014.

Hugo Touvron, Matthieu Cord, Matthijs Douze, Francisco Massa, Alexandre Sablayrolles, and Hervé Jégou. Training data-efficient image transformers & distillation through attention. In *International conference on machine learning*, pp. 10347–10357. PMLR, 2021.

Chenxi Wang, Hongjun Wu, and Zhi Jin. Fourllie: Boosting low-light image enhancement by fourier frequency information. In *Proceedings of the 31st ACM International Conference on Multimedia*, pp. 7459–7469, 2023a.

Jianyi Wang, Kelvin CK Chan, and Chen Change Loy. Exploring clip for assessing the look and feel of images. In *Proceedings of the AAAI conference on artificial intelligence*, volume 37, pp. 2555–2563, 2023b.

Ruixing Wang, Qing Zhang, Chi-Wing Fu, Xiaoyong Shen, Wei-Shi Zheng, and Jiaya Jia. Underexposed photo enhancement using deep illumination estimation. In *Proceedings of the IEEE/CVF conference on computer vision and pattern recognition*, pp. 6849–6857, 2019.

Shuhang Wang, Jin Zheng, Hai-Miao Hu, and Bo Li. Naturalness preserved enhancement algorithm for non-uniform illumination images. *IEEE transactions on image processing*, 22(9):3538–3548, 2013.

Wenhui Wang, Furu Wei, Li Dong, Hangbo Bao, Nan Yang, and Ming Zhou. Minilm: Deep self-attention distillation for task-agnostic compression of pre-trained transformers. *Advances in neural information processing systems*, 33:5776–5788, 2020.

Yinglong Wang, Zhen Liu, Jianzhuang Liu, Songcen Xu, and Shuaicheng Liu. Low-light image enhancement with illumination-aware gamma correction and complete image modelling network. In *Proceedings of the IEEE/CVF International Conference on Computer Vision*, pp. 13128–13137, 2023c.

Yufei Wang, Renjie Wan, Wenhan Yang, Haoliang Li, Lap-Pui Chau, and Alex Kot. Low-light image enhancement with normalizing flow. In *Proceedings of the AAAI conference on artificial intelligence*, volume 36, pp. 2604–2612, 2022.

Chen Wei, Wenjing Wang, Wenhan Yang, and Jiaying Liu. Deep retinex decomposition for low-light enhancement. *arXiv preprint arXiv:1808.04560*, 2018.

Wenhui Wu, Jian Weng, Pingping Zhang, Xu Wang, Wenhan Yang, and Jianmin Jiang. Uretinex-net: Retinex-based deep unfolding network for low-light image enhancement. In *Proceedings of the IEEE/CVF conference on computer vision and pattern recognition*, pp. 5901–5910, 2022.

Bin Xia, Yulun Zhang, Shiyin Wang, Yitong Wang, Xinglong Wu, Yapeng Tian, Wenming Yang, and Luc Van Gool. Diffir: Efficient diffusion model for image restoration. In *Proceedings of the IEEE/CVF international conference on computer vision*, pp. 13095–13105, 2023.

Xiaogang Xu, Ruixing Wang, Chi-Wing Fu, and Jiaya Jia. Snr-aware low-light image enhancement. In *Proceedings of the IEEE/CVF conference on computer vision and pattern recognition*, pp. 17714–17724, 2022.

Qingsen Yan, Yixu Feng, Cheng Zhang, Pei Wang, Peng Wu, Wei Dong, Jinqiu Sun, and Yanning Zhang. You only need one color space: An efficient network for low-light image enhancement. *arXiv preprint arXiv:2402.05809*, 2024.

Qingsen Yan, Kangbiao Shi, Yixu Feng, Tao Hu, Peng Wu, Guansong Pang, and Yanning Zhang. Hvi-cidnet+: Beyond extreme darkness for low-light image enhancement. *arXiv preprint arXiv:2507.06814*, 2025.

Ling Yang, Zixiang Zhang, Zhilong Zhang, Xingchao Liu, Minkai Xu, Wentao Zhang, Chenlin Meng, Stefano Ermon, and Bin Cui. Consistency flow matching: Defining straight flows with velocity consistency. *arXiv preprint arXiv:2407.02398*, 2024.

Shuzhou Yang, Moxuan Ding, Yanmin Wu, Zihan Li, and Jian Zhang. Implicit neural representation for cooperative low-light image enhancement. In *Proceedings of the IEEE/CVF international conference on computer vision*, pp. 12918–12927, 2023.

Wenhan Yang, Wenjing Wang, Haofeng Huang, Shiqi Wang, and Jiaying Liu. Sparse gradient regularized deep retinex network for robust low-light image enhancement. *IEEE Transactions on Image Processing*, 30:2072–2086, 2021.

Xunpeng Yi, Han Xu, Hao Zhang, Linfeng Tang, and Jiayi Ma. Diff-retinex: Rethinking low-light image enhancement with a generative diffusion model. In *Proceedings of the IEEE/CVF international conference on computer vision*, pp. 12302–12311, 2023.

Sergey Zagoruyko and Nikos Komodakis. Paying more attention to attention: Improving the performance of convolutional neural networks via attention transfer. *arXiv preprint arXiv:1612.03928*, 2016.

Syed Waqas Zamir, Aditya Arora, Salman Khan, Munawar Hayat, Fahad Shahbaz Khan, Ming-Hsuan Yang, and Ling Shao. Learning enriched features for fast image restoration and enhancement. *IEEE transactions on pattern analysis and machine intelligence*, 45(2):1934–1948, 2022.

Yonghua Zhang, Jiawan Zhang, and Xiaojie Guo. Kindling the darkness: A practical low-light image enhancer. In *Proceedings of the 27th ACM international conference on multimedia*, pp. 1632–1640, 2019.

Zizhao Zhang, Han Zhang, Long Zhao, Ting Chen, Sercan Ö Arik, and Tomas Pfister. Nested hierarchical transformer: Towards accurate, data-efficient and interpretable visual understanding. In *Proceedings of the AAAI Conference on Artificial Intelligence*, volume 36, pp. 3417–3425, 2022.

Naishan Zheng, Man Zhou, Yanmeng Dong, Xiangyu Rui, Jie Huang, Chongyi Li, and Feng Zhao. Empowering low-light image enhancer through customized learnable priors. In *Proceedings of the IEEE/CVF International Conference on Computer Vision*, pp. 12559–12569, 2023.

Shen Zheng, Yiling Ma, Jinqian Pan, Changjie Lu, and Gaurav Gupta. Low-light image and video enhancement: A comprehensive survey and beyond. *arXiv preprint arXiv:2212.10772*, 2022.

Jingchun Zhou, Qian Liu, Qiuping Jiang, Wenqi Ren, Kin-Man Lam, and Weishi Zhang. Underwater camera: Improving visual perception via adaptive dark pixel prior and color correction. *International Journal of Computer Vision*, pp. 1–19, 2023.

Shangchen Zhou, Chongyi Li, and Chen Change Loy. Lednet: Joint low-light enhancement and deblurring in the dark. In *European conference on computer vision*, pp. 573–589. Springer, 2022.

Shihao Zhou, Duosheng Chen, Jinshan Pan, Jinglei Shi, and Jufeng Yang. Adapt or perish: Adaptive sparse transformer with attentive feature refinement for image restoration. In *Proceedings of the IEEE/CVF conference on computer vision and pattern recognition*, pp. 2952–2963, 2024.

A APPENDIX

A.1 ETHICS STATEMENT

LLMs were only used for editorial assistance and polishing grammar for the manuscript, with no participation in technical interpretation, or content development.

A.2 REPRODUCIBILITY STATEMENT

Code and pretrained model weights will be released upon acceptance.

A.3 BROADER IMPACT

Efficient image restoration has positive applications in medical imaging, autonomous systems, and accessibility. No significant negative societal impacts are identified by us.

A.4 THEORETICAL JUSTIFICATION OF FLEX LOSS

We provide theoretical justification for FLEX's key design choices to ensure stable optimization dynamics.

Assumption 1 (Feature Boundedness): Teacher and student features are bounded during training: $\|\mathbf{f}^l_{\text{teach}}\|, \|\mathbf{f}^l_{\text{stud}}\| \leq M$ for some constant $M > 0$.

Assumption 2 (Non-degeneracy): Student feature standard deviations satisfy $\sigma^l_{\text{stud}} \geq \sigma_{\min} > 0$ to prevent division by zero in normalization.

Claim 1 Cross-normalization using student statistics prevents gradient explosion when teacher and student features have different scales.

Justification: Standard feature matching $L = \|\mathbf{f}_{\text{teach}} - \mathbf{f}_{\text{stud}}\|^2$ produces gradients proportional to $(\mathbf{f}_{\text{teach}} - \mathbf{f}_{\text{stud}})$. When teacher features are much larger than student features, this difference can be arbitrarily large, causing unstable training.

FLEX cross-normalization ensures both normalized features have the same scale:

$$\mathbf{f}^{\text{norm}}_{\text{teach}} = \frac{\mathbf{f}_{\text{teach}} - \mu_{\text{stud}}}{\sigma_{\text{stud}}}, \quad \mathbf{f}^{\text{norm}}_{\text{stud}} = \frac{\mathbf{f}_{\text{stud}} - \mu_{\text{stud}}}{\sigma_{\text{stud}}} \tag{6}$$

Both normalized features have bounded variance, preventing gradient explosion regardless of the original scale mismatch.

Claim 2 Percentile-based masking provides robustness to feature corruption.

Justification: By masking extreme values above the p-th percentile (default $p = 95\%$), FLEX focuses learning on reliable feature regions. If corruption affects only a small fraction of spatial locations, most corrupted features will exceed the percentile threshold and be masked out. By excluding the top 5% extreme activations, FLEX prevents gradient dominance by outliers, ensuring that meaningful feature patterns rather than numerical instabilities drive the optimization.

For corruption affecting $\alpha < (100 - p)/100$ of spatial locations, the outlier detection will identify and exclude most corrupted regions, limiting their impact on the overall loss.

Claim 3 The resolution weighting $w^{\text{res}}_l = \max\left((H_{\text{base}} W_{\text{base}} / H_l W_l)^{0.25}, 0.1\right)$ balances multi-scale contributions.

Justification: Higher resolution features contain more spatial elements, potentially dominating the loss. The inverse relationship with spatial resolution prevents this dominance. The 0.25 exponent provides gradual rather than aggressive down-weighting, preserving fine-grained information while preventing over-emphasis on high-resolution layers.

A.5 Theoretical Justification of Rectified Flow for Knowledge Distillation

We provide theoretical grounding for reformulating knowledge distillation as a rectified flow process.

Rectified Flow Formulation: For teacher features $\mathbf{f}_{\text{teach}}$ and noise $\mathbf{z} \sim \mathcal{N}(0, \mathbf{I})$, we define the linear interpolation path:

$$\mathbf{x}_t = (1-t)\mathbf{z} + t\mathbf{f}_{\text{teach}}, \quad t \in [0,1] \tag{7}$$

The corresponding velocity field is:

$$\mathbf{v}(\mathbf{x}_t, t) = \frac{d\mathbf{x}_t}{dt} = \mathbf{f}_{\text{teach}} - \mathbf{z} \tag{8}$$

The student network learns a velocity predictor $\mathbf{v}_\theta(\mathbf{x}_t, t)$ by minimizing:

$$L_{\text{vel}} = \mathbb{E}_{t,\mathbf{z},\mathbf{f}_{\text{teach}}} \left[\|\mathbf{v}_\theta(\mathbf{x}_t, t) - \mathbf{v}(\mathbf{x}_t, t)\|_2^2 \right] \tag{9}$$

Claim 4 (Transport Cost Reduction): Learning rectified flow reduces convex transport costs compared to arbitrary couplings between noise and target features.

Justification: Following Liu et al. (2022), the rectified flow procedure transforms an arbitrary coupling between distributions into a deterministic coupling with provably non-increasing convex transport costs. Specifically, for any convex cost function c, the expected cost $\mathbb{E}[c(\mathbf{f}_{\text{teach}} - \mathbf{z})]$ is reduced through the straight-line parameterization. This property ensures that the student learns an efficient transport map from noise to teacher-quality features, which is more sample-efficient than curved trajectories used in diffusion-based distillation methods like DDIM.

Claim 5 (Exact Simulation without Discretization): Straight-line ODEs can be solved exactly with Euler integration, enabling few-step inference.

Justification: The velocity field $\mathbf{v}(\mathbf{x}_t, t) = \mathbf{f}_{\text{teach}} - \mathbf{z}$ is constant along the trajectory, making the ODE solution exact: $\mathbf{x}_1 = \mathbf{x}_0 + \int_0^1 \mathbf{v}(\mathbf{x}_t, t)dt = \mathbf{z} + (\mathbf{f}_{\text{teach}} - \mathbf{z}) = \mathbf{f}_{\text{teach}}$. This means Euler integration with step size Δt incurs zero discretization error for perfectly straight paths. In practice, the learned velocity predictor $\mathbf{v}_\theta$ approximates this constant field, allowing accurate simulation with as few as 1-4 steps. In contrast, curved trajectories (e.g., DDIM's probability flow ODE) require many more steps to achieve similar accuracy, as shown empirically in Figure 3 where our method achieves lower FID with 4 steps than DDIM with 10 steps.

A.6 Architecture Choice Justification

Using separate networks for low-light and normal-light images ensures robust Retinex decomposition across illumination conditions. As reported by Reti-Diff and Diff-IR, a single adaptive network would require more complex conditioning mechanisms. The two-phase student training approach addresses fundamental optimization challenges in generative knowledge distillation. Phase separation prevents objective conflicts as simultaneously learning velocity prediction and image reconstruction creates competing gradients. The velocity predictor tries to match teacher feature distributions while the reconstruction network optimizes for pixel-level accuracy. These objectives can work against each other, leading to suboptimal solutions. Feature space stabilization where Phase 1 establishes stable feature generation capabilities before introducing reconstruction complexity. This ensures the velocity predictors learn meaningful feature trajectories rather than shortcuts that minimize reconstruction error. Only the student network is deployed during inference, with no additional computational overhead compared to baseline restoration networks.

For SNR threshold (0.4), we notice performance remains stable within ±0.2 range. The threshold determines when FLEX loss is applied - too low (0.2) restricts learning, too high (0.8) includes noisy states. For outlier percentile value, we found that lower percentiles (90%) are more aggressive in outlier detection but may remove useful information. Higher percentiles (99%) retain more data but include potential artifacts. For resolution weighting exponent value (0.25), we notice values from 0.125-0.5 show similar performance. This parameter balances multi-scale contributions as lower values provide gentler weighting while higher values more aggressively down-weight high-resolution features.

Standard layer normalization operates on channel dimensions independently, losing spatial correlations crucial for restoration tasks. SCLN computes global statistics across both spatial and channel dimensions, capturing holistic image characteristics while maintaining learnable channel-wise scaling. Degraded images contain irregular noise patterns that can cause attention weight saturation. Normalizing Q and K before attention computation prevents extreme attention weights and ensures stable gradient flow. The ”RestoRect w/o SCLN” ablation (red curve in Figure 3) essentially represents the RetiDiff baseline architecture using standard layer normalization, providing direct comparison between our architectural innovations and existing methods. FLEX loss becomes more critical for cross-domain scenarios, as feature distribution mismatches are more severe between different datasets than within-dataset variations. On modern GPUs (RTX 4090/H100), the difference between 3-step (156ms) and 5-step (198ms) inference is minimal compared to the quality improvement. The 5-step choice during inference optimizes the quality-practicality trade-off for real-world deployment across different types of datasets.

A.7 Architecture Overview

RestoRect implements a two-stage knowledge distillation framework for efficient image restoration. Given degraded input $I_{LQ} \in \mathbb{R}^{H\times W\times 3}$ and ground truth $I_{GT} \in \mathbb{R}^{H\times W\times 3}$, the objective is:

$$\mathcal{F}_S(I_{LQ}) \approx \mathcal{F}_T(I_{LQ}) \approx I_{GT}$$

where $\mathcal{F}_T$ represents the teacher network (Stage 1) and $\mathcal{F}_S$ the student network (Stage 2).

A.7.1 Retinex Decomposition Networks

The Retinex decomposition models an image as the product of reflectance and illumination:

$$I = R \odot L$$

Two decomposition networks $\mathcal{D}_l$ (low-light) and $\mathcal{D}_h$ (normal-light) map:

$$\mathcal{D}(I) \to (R, L)$$

where $R \in \mathbb{R}^{H\times W\times 3}$ and $L \in \mathbb{R}^{H\times W\times 1}$.

Network Architecture:

$$\begin{aligned}\text{Decom}(I) =& \text{ReLU}(\text{Conv2d}^{3\times 3}_{32\to 4}(\\ &\text{LeakyReLU}_{0.2}(\text{Conv2d}^{3\times 3}_{32\to 32}(\\ &\text{LeakyReLU}_{0.2}(\text{Conv2d}^{3\times 3}_{32\to 32}(\\ &\text{LeakyReLU}_{0.2}(\text{Conv2d}^{3\times 3}_{3\to 32}(I))))))\end{aligned} \tag{10}$$

Output split: $R = \text{output}[:, 0:3, :, :]$, $L = \text{output}[:, 3:4, :, :]$

A.7.2 Feature Encoders

Retinex ResNet Encoder (RRE) The RRE processes retinex features through separate reflectance and illumination pathways:

Input Processing:

$$\begin{aligned}\text{Retinex}_{LQ} &= [R_{lq}; L_{lq}] \in \mathbb{R}^{H\times W\times 4}\\ \text{Retinex}_{GT} &= [R_{gt}; L_{gt}] \in \mathbb{R}^{H\times W\times 4}\end{aligned}$$

Pixel Unshuffle:

$$\text{X}_0 = \text{PixelUnshuffle}_4(\text{Retinex}) \in \mathbb{R}^{H/4\times W/4\times 64}$$

Channel Split:

$$X_R = \text{X}_0[:, 0:48, :, :] \quad \text{(Reflectance channels)} \tag{11}$$

$$X_I = \text{X}_0[:, 48:64, :, :] \quad \text{(Illumination channels)} \tag{12}$$

Reflectance Branch (E_R):

$$\begin{aligned}E_R(X_R \oplus X_{R,gt}) =& \text{AdaptiveAvgPool2d}(\\ &\text{LeakyReLU}_{0.1}(\text{Conv2d}^{3\times 3}_{128\to 192}(\\ &\text{LeakyReLU}_{0.1}(\text{Conv2d}^{3\times 3}_{128\to 128}(\\ &\text{LeakyReLU}_{0.1}(\text{Conv2d}^{3\times 3}_{64\to 128}(\\ &\text{ResBlock}^{6}(\text{LeakyReLU}_{0.1}(\text{Conv2d}^{3\times 3}_{96\to 64}(\\ &X_R \oplus X_{R,gt}))))))))\end{aligned} \tag{13}$$

Illumination Branch (E_I):

$$\begin{aligned} E_I(X_I \oplus X_{I,gt}) = &\text{AdaptiveAvgPool2d}(\\ &\text{LeakyReLU}_{0.1}(\text{Conv2d}^{3\times3}_{128\to64}(\\ &\text{LeakyReLU}_{0.1}(\text{Conv2d}^{3\times3}_{128\to128}(\\ &\text{LeakyReLU}_{0.1}(\text{Conv2d}^{3\times3}_{64\to128}(\\ &\text{ResBlock}^{6}(\text{LeakyReLU}_{0.1}(\text{Conv2d}^{3\times3}_{32\to64}(\\ &X_I \oplus X_{I,gt}))))))) \end{aligned} \tag{14}$$

Feature Fusion:

$$\text{feat}_R = \text{MLP}_R(E_R(\text{output})) \in \mathbb{R}^{192} \tag{15}$$

$$\text{feat}_I = \text{MLP}_I(E_I(\text{output})) \in \mathbb{R}^{64} \tag{16}$$

$$\text{IPR}_{rex} = [\text{feat}_R; \text{feat}_I] \in \mathbb{R}^{256} \tag{17}$$

Image ResNet Encoder (IRE) The IRE processes raw image features:

Input Processing:

$$\text{X}_{LQ} = \text{PixelUnshuffle}_4(I_{LQ}) \in \mathbb{R}^{H/4\times W/4\times 48} \tag{18}$$

$$\text{X}_{GT} = \text{PixelUnshuffle}_4(I_{GT}) \in \mathbb{R}^{H/4\times W/4\times 48} \tag{19}$$

$$\text{X}_{concat} = [\text{X}_{LQ}; \text{X}_{GT}] \in \mathbb{R}^{H/4\times W/4\times 96} \tag{20}$$

Encoder Architecture:

$$\begin{aligned} E(\text{X}_{concat}) = &\text{AdaptiveAvgPool2d}(\\ &\text{LeakyReLU}_{0.1}(\text{Conv2d}^{3\times3}_{128\to256}(\\ &\text{LeakyReLU}_{0.1}(\text{Conv2d}^{3\times3}_{128\to128}(\\ &\text{LeakyReLU}_{0.1}(\text{Conv2d}^{3\times3}_{64\to128}(\\ &\text{ResBlock}^{6}(\text{LeakyReLU}_{0.1}(\text{Conv2d}^{3\times3}_{96\to64}(\\ &\text{X}_{concat}))))))) \end{aligned} \tag{21}$$

Output:

$$\text{IPR}_{img} = \text{LayerNorm}(\text{MLP}(E(\text{output}))) \in \mathbb{R}^{256}$$

A.7.3 UNet Transformer Architecture

Spatial Channel Layer Normalization (SCLN) SCLN captures global image statistics across spatial and channel dimensions:

$$\mu_{global} = \frac{1}{B \cdot C \cdot H \cdot W} \sum_{b,c,h,w} x_{b,c,h,w} \tag{22}$$

$$\sigma^2_{global} = \frac{1}{B \cdot C \cdot H \cdot W} \sum_{b,c,h,w} (x_{b,c,h,w} - \mu_{global})^2 \tag{23}$$

$$\text{SCLN}(x) = \frac{x - \mu_{global}}{\sqrt{\sigma^2_{global} + \epsilon}} \cdot \gamma \tag{24}$$

where $\gamma \in \mathbb{R}^C$ is learnable channel-wise scaling.

Retinex Attention The Retinex attention mechanism uses separate conditioning for reflectance and illumination components:

Feature Conditioning:

$$k_{v_r} = \text{Linear}(k_v[0:192]) \in \mathbb{R}^{3C/4\times1\times1} \tag{25}$$

$$k_{v_i} = \text{Linear}(k_v[192:256]) \in \mathbb{R}^{C/4\times1\times1} \tag{26}$$

$$x_r = x[:, 0:3C/4, :, :] \odot k_{v_r} + x[:, 0:3C/4, :, :] \tag{27}$$

$$x_i = x[:, 3C/4:C, :, :] \odot k_{v_i} + x[:, 3C/4:C, :, :] \tag{28}$$

Query-Key-Value Computation:

$$Q = \text{DepthwiseConv}(\text{Conv}(x_r)) \in \mathbb{R}^{B\times C\times H\times W} \tag{29}$$

$$KV = \text{DepthwiseConv}(\text{Conv}(x_i)) \in \mathbb{R}^{B\times 2C\times H\times W} \tag{30}$$

$$K, V = \text{split}(KV, \text{dim} = 1) \tag{31}$$

Attention with QK Normalization:

$$Q_{norm} = \text{LayerNorm}(Q), \quad K_{norm} = \text{LayerNorm}(K) \tag{32}$$

$$Q_{norm} = \frac{Q_{norm}}{\|Q_{norm}\|_2}, \quad K_{norm} = \frac{K_{norm}}{\|K_{norm}\|_2} \tag{33}$$

$$\text{Attn} = \text{softmax}\left(\frac{Q_{norm} \cdot K_{norm}^T}{\sqrt{d_k}} \cdot \tau\right) \tag{34}$$

$$\text{Output} = \text{Attn} \cdot V \tag{35}$$

where τ is a learnable temperature parameter.

Multi-Scale U-Net Architecture Encoder Path:

$$\text{Level 1:} \quad [B, 48, H, W] \xrightarrow{4\times\text{TransformerBlock}} [B, 48, H, W] \tag{36}$$

$$\downarrow \text{Downsample} \tag{37}$$

$$\text{Level 2:} \quad [B, 96, H/2, W/2] \xrightarrow{6\times\text{TransformerBlock}} [B, 96, H/2, W/2] \tag{38}$$

$$\downarrow \text{Downsample} \tag{39}$$

$$\text{Level 3:} \quad [B, 192, H/4, W/4] \xrightarrow{6\times\text{TransformerBlock}} [B, 192, H/4, W/4] \tag{40}$$

$$\downarrow \text{Downsample} \tag{41}$$

$$\text{Level 4:} \quad [B, 384, H/8, W/8] \xrightarrow{8\times\text{TransformerBlock}} [B, 384, H/8, W/8] \tag{42}$$

Decoder Path with Skip Connections:

$$\text{Level 3:} \quad \text{Upsample} + \text{Concat} + \text{ReduceChannel} \xrightarrow{6\times\text{TransformerBlock}} \tag{43}$$

$$\text{Level 2:} \quad \text{Upsample} + \text{Concat} + \text{ReduceChannel} \xrightarrow{6\times\text{TransformerBlock}} \tag{44}$$

$$\text{Level 1:} \quad \text{Upsample} + \text{Concat} \xrightarrow{4\times\text{TransformerBlock}} \tag{45}$$

$$\xrightarrow{4\times\text{TransformerBlock}} \text{Conv2d}(96 \to 3) + \text{Residual} \tag{46}$$

A.7.4 Auxiliary Constraints

Anisotropic Diffusion The anisotropic diffusion operator preserves edges while smoothing noise:

$$\mathcal{A}(I) = \nabla \cdot (c(|\nabla I|)\nabla I)$$

with diffusion coefficient:

$$c(|\nabla I|) = \exp\left(-\frac{|\nabla I|^2}{s^2}\right)$$

where $s \in [0.01, 1.0]$ is a learnable sensitivity parameter.

Texture Consistency Loss:

$$L_{tex} = \|\mathcal{A}(I_{input}) - \mathcal{A}(R_{pred})\|_1$$

Illumination Smoothness Loss:

$$L_{lum} = \sum_{i,j} w_{i,j} \left(|\nabla_x L_{i,j}|^2 + |\nabla_y L_{i,j}|^2 \right)$$

where $w_{i,j} = \exp(-|\nabla L_{i,j}|)$ provides gradient-aware weighting.

Polarized HVI Color Space The polarized HVI transformation eliminates red discontinuity:

$$H_{polar} = C_k \cdot S \cdot \cos(\pi H/3) \tag{47}$$
$$V_{polar} = C_k \cdot S \cdot \sin(\pi H/3) \tag{48}$$
$$I_{polar} = I_{max} = \max(R, G, B) \tag{49}$$

where the adaptive intensity collapse factor is:

$$C_k = k \cdot \sin(\pi I_{max}/2) + \epsilon$$

with learnable parameter $k \in [0.1, 5.0]$.

Polarized Color Loss:

$$L_{col} = \|H^{pred}_{polar} - H^{gt}_{polar}\|_1 + \|V^{pred}_{polar} - V^{gt}_{polar}\|_1 + \|I^{pred}_{polar} - I^{gt}_{polar}\|_1$$

A.7.5 Teacher Training Objective

The complete teacher training loss combines:

$$L_{teach} = L_{rec} + L_{vgg} + L_{sty} + \lambda_{tex} L_{tex} + \lambda_{col} L_{col} + \lambda_{lum} L_{lum}$$

where:

$$L_{rec} = \|I_{pred} - I_{gt}\|_1 \quad \text{(pixel loss)} \tag{50}$$
$$L_{vgg} = \sum_l \lambda_l \|\phi_l(I_{pred}) - \phi_l(I_{gt})\|_2^2 \quad \text{(perceptual loss)} \tag{51}$$
$$L_{sty} = \sum_l \|G_l(\phi_l(I_{pred})) - G_l(\phi_l(I_{gt}))\|_F^2 \quad \text{(style loss)} \tag{52}$$

with $\lambda_{tex} = 0.05$, $\lambda_{col} = 0.05$, $\lambda_{lum} = 0.2$.

A.8 Stage 2: Student Network Architecture

A.8.1 Rectified Flow Formulation

Rectified flow models feature synthesis through straight-line interpolation:

$$\mathbf{x}_t = (1-t)\mathbf{z} + t\mathbf{f}_{teach}, \quad t \in [0, 1]$$

where $\mathbf{z} \sim \mathcal{N}(0, I)$ is noise and $\mathbf{f}_{teach}$ are teacher features.

Velocity Field:

$$\mathbf{v}(\mathbf{x}_t, t) = \frac{d\mathbf{x}_t}{dt} = \mathbf{f}_{teach} - \mathbf{z}$$

A.8.2 VELOCITY PREDICTION NETWORKS

Architecture for both ϵ_θ^{rex} and ϵ_θ^{img}:

$$\begin{aligned}\text{VelocityPredictor}(\mathbf{x}_t, t, \mathbf{c}) = &\text{ResMLP}^5(\\ &\text{LeakyReLU}_{0.1}(\text{Linear}_{513\to256}(\\ &[\mathbf{c}; t_{norm}; \mathbf{x}_t])))\end{aligned} \tag{53}$$

where the input is $[\mathbf{c}; t; \mathbf{x}_t] \in \mathbb{R}^{513}$ with time normalization $t_{norm} = t/t_{max}$.

Velocity Matching Loss:

$$L_{vel} = \mathbb{E}_{t,\mathbf{z},\mathbf{f}_{teach}}\left[\|\epsilon_\theta(\mathbf{x}_t, t, \mathbf{c}) - \mathbf{v}(\mathbf{x}_t, t)\|_2^2\right]$$

A.8.3 ODE INTEGRATION FOR INFERENCE

During inference, the ODE is solved using Euler's method:

$$\mathbf{x}_{t+\Delta t} = \mathbf{x}_t + \Delta t \cdot \epsilon_\theta(\mathbf{x}_t, t, \mathbf{c})$$

with adaptive step sizing $\Delta t = 1.0/N_{steps}$ for $N_{steps} \in [1, 5]$.

A.8.4 FLEX KNOWLEDGE DISTILLATION LOSS

Cross-Normalization FLEX uses student statistics for normalizing both teacher and student features at each layer l:

$$\mu_{stud}^l = \frac{1}{H_l W_l}\sum_{h,w}\mathbf{f}_{stud}^{l,h,w} \tag{54}$$

$$\sigma_{stud}^l = \sqrt{\frac{1}{H_l W_l}\sum_{h,w}(\mathbf{f}_{stud}^{l,h,w} - \mu_{stud}^l)^2 + \epsilon} \tag{55}$$

$$\mathbf{f}_{teach}^{l,norm} = \frac{\mathbf{f}_{teach}^l - \mu_{stud}^l}{\sigma_{stud}^l} \tag{56}$$

$$\mathbf{f}_{stud}^{l,norm} = \frac{\mathbf{f}_{stud}^l - \mu_{stud}^l}{\sigma_{stud}^l} \tag{57}$$

Percentile-Based Outlier Detection For each layer l and channel c, we compute:

$$\tau_p^{l,c} = \text{Percentile}(|\mathbf{f}_{stud}^{l,c,norm}|, p) \tag{58}$$

$$M_{reliable}^{l,c,h,w} = \mathbb{I}[|\mathbf{f}_{stud}^{l,c,norm,h,w}| \le \tau_p^{l,c}] \tag{59}$$

where $p = 95\%$ is the outlier percentile threshold.

Resolution-Aware Weighting Dynamic resolution weighting prevents high-resolution features from dominating:

$$w_l^{res} = \max\left(\left(\frac{H_{base}W_{base}}{H_l W_l}\right)^{0.25}, 0.1\right) \tag{60}$$

where $(H_{base}, W_{base}) = (64, 64)$ and (H_l, W_l) is the spatial resolution at layer l.

Complete FLEX Loss The final FLEX loss combines masked feature matching with dual weighting:

$$L_{FLEX} = \sum_l w_l^{layer} \cdot w_l^{res} \cdot \frac{\sum_{c,h,w} M_{reliable}^{l,c,h,w} \cdot \|\mathbf{f}_{teach}^{l,c,norm,h,w} - \mathbf{f}_{stud}^{l,c,norm,h,w}\|^2}{\sum_{c,h,w} M_{reliable}^{l,c,h,w} + \epsilon} \tag{61}$$

where w_l^{layer} are predefined layer importance weights and the denominator normalizes by the number of reliable (non-outlier) elements.

A.8.5 TRAJECTORY CONSISTENCY REGULARIZATION

Smooth Transitions:

$$L_{trans} = \sum_{i=1}^{N-1} \|\mathbf{f}_{pred}^{i+1} - \mathbf{f}_{pred}^{i}\|_2^2$$

Target Alignment:

$$L_{target} = \|\mathbf{f}_{pred}^{final} - \mathbf{f}_{teach}\|_2^2$$

Semantic Consistency:

$$L_{cons} = \sum_{i=1}^{N} \text{cos\_dist}(\mathbf{f}_{pred}^{i}, \mathbf{f}_{teach})$$

Complete Trajectory Loss:

$$L_{traj} = \alpha_{trans} L_{trans} + \alpha_{target} L_{target} + \alpha_{cons} L_{cons}$$

with $\alpha_{trans} = 0.1$, $\alpha_{target} = 0.5$, $\alpha_{cons} = 0.2$.

A.8.6 TWO-PHASE TRAINING PROTOCOL

Phase 1: Velocity Learning

$$L_{phase1} = L_{vel}^{rex} + L_{vel}^{img} + \lambda_{KD} L_{KD} + \lambda_{traj} L_{traj}$$

Phase 2: Full Network Training

$$L_{phase2} = L_{rec} + \lambda_{FLEX} L_{FLEX} + \lambda_{vel}(L_{vel}^{rex} + L_{vel}^{img})$$

with $\lambda_{FLEX} = 0.15$, $\lambda_{vel} = 0.05$.

A.9 IMPLEMENTATION DETAILS

A.9.1 NETWORK DIMENSIONS AND PARAMETERS

Stage 1 (Teacher):

- RGFormer dimensions: dim $= 48$
- Multi-head attention heads: $[1, 2, 4, 8]$
- Transformer blocks per level: $[4, 6, 6, 8]$
- FFN expansion factor: 2.66

Stage 2 (Student):

- Velocity predictor features: 256
- Rectified flow timesteps: 4
- ODE integration steps: $1 - 5$

A.9.2 TRAINING HYPERPARAMETERS

Stage 1:

- Learning rate: 2×10^{-4}
- Batch size: 16
- Training iterations: $500k$

Stage 2:

- Phase 1 learning rates: $lr_{rex} = lr_{img} = 2 \times 10^{-4}$
- Phase 2 learning rate: 1×10^{-4}
- Phase 1 iterations: $50k$
- Phase 2 iterations: $200k$